Electrical conductivity of Icelandic deep geothermal reservoirs up to supercritical conditions: Insight from laboratory experiments

Franck Nono, Benoit Gibert, Fleurice Parat, Didier Loggia, Sarah Cichy, Marie Estelle Solange Violay

Electrical conductivity of Icelandic deep geothermal reservoirs up to supercritical conditions: insight from laboratory experiments

Franck Nono[1,2], Benoit Gibert[1], Fleurice Parat[1], Didier Loggia[1], Sarah B. Cichy[3,4] and Marie Violay[5].

(1) University of Montpellier, Laboratoire Géosciences, Montpellier, France.

(2) University of Pau, UMS-DMEX, Pau, France.

(3) University of Potsdam, Potsdam, Germany.

(4) GFZ German Research Centre for Geosciences, Postdam, Germany.

(5) LEMR, ENAC, Ecole Polytechnique Fédérale de Lausanne, Lausanne, Suisse.

Corresponding author: Franck Nono, franck.nono@univ-pau.fr

ABSTRACT

Electrical resistivity is extensively used in geothermal systems to accurately determine the existing conditions of the reservoirs at depth. Up to this point, technical challenges related to pore fluid confinement made difficult to measure electrical conductivity at temperatures and pressures representative of very deep geothermal reservoirs. In this study, we are overcoming these limitations thanks to a new electrical resistivity cell designed to fit into a high temperature gas medium apparatus. This allows us to perform resistivity measurement at temperatures up to 700°C and at effective pressures up to 100 MPa (i.e. a confining pressure of 130 MPa and an equilibrium pore pressure of 30MPa) using cm-scale plugs. Rock samples originate from five boreholes located in the Icelandic geothermal fields of Reykjanes (RN-17B/Hyaloclastite,

RN-19/RN-30/dolerites) and Hengill (NJ-17/basalt and NJ-17B/Hyaloclastite). These samples were selected for their high degree of hydrothermal alteration in the epidote and amphibole facies (i.e. temperature of 250°C and 400°C respectively), and their wide range of porosities (from 3% to 20%). To determine the effects of surface, mineral and electrolytic conductions on bulk electrical conduction, experiments were performed under dry and saturated conditions using three different fluid salinities.

At temperatures ranging from 25 to ~ 350°C, electrical conductivity in all our experiments increases as a result of both increasing surface and electrolytic conduction. Then, under supercritical conditions, i.e. temperature from 374°C to 600°C, electrical conductivity strongly decreases due to the evolution of water density and dielectric constant that affect both surface and electrolyte conduction. At higher temperatures (500°C – 700°C), the rock conductivities lie within the range of dry rock electrical conductivity values, suggesting that mineral conduction controls the bulk conductivity with ferromagnesian minerals acting as principal contributors of mineral conduction. Amphibole-rich samples show an irreversible increase in conductivity at temperature above 500°C-600°C, which can be attributed to amphibole dehydration. Comparison of these laboratory data to magnetotelluric soundings and downhole temperatures obtained beneath several geothermal areas indicate a good agreement between laboratory and large-scale surveys. Our results provide a general trend that helps interpreting electrical conductivity surveys in the Icelandic crust.

Keywords: water supercritical conditions, deep geothermal reservoirs, electrical conductivity, alteration minerals.

1. Introduction

Geothermal energy is a green, renewable energy and a good alternative to fossil fuel energy. While low temperature geothermal energy is used to supply heating to buildings and is accessible almost everywhere on earth, high temperature geothermal energy (T > 200°C) used for electrical production remains limited to specific geographic areas. In particular, Iceland is one of the most dynamic volcanic and tectonic regions in the world where heat and fluids reach depths closer to Earth's surface. This leads to high temperature gradients at shallow depth (100°C/km) and thus a favorable enthalpy for electrical energy generation. In these volcanic regions, conventional wells are used to extract fluids at temperature < 300°C, i.e. the power capacity per well is limited to about 5-10 MW. However, recent simulations expect a net increase of the power extracted from deep geothermal reservoirs by exploiting supercritical fluids by a factor of 5 to 10 (e.g. Friðleifsson and Elders, 2005). Following these estimations, supercritical reservoirs could become one of the most important sources of sustainable energy for electrical generation.

A supercritical fluid is defined as any phase at conditions above its critical point (P, T), where distinct liquid and gas phases do not exist. Supercritical water occurs at temperatures and pressures higher than 374°C and 22 MPa for pure water, and higher than 406°C and 30 MPa for sea water. At these conditions, water acts as a single phase and its physical properties are such that viscosity may remain very low (gas like) while its density may be close to a liquid-like density, allowing for enhanced mass and energy transfer (e.g. Fournier, 1999, Friedleifsson and Elders, 2005). These supercritical reservoirs can be located at few km depths where important heat sources such as cooling magmas and fluid pathways may be combined and potentially preserved over exploitation durations (e.g. Elders et al., 2014, Scott et al., 2015). In Iceland, given the temperature gradient observed in geothermal areas and considering that fluid pressure is hydrostatic, such conditions could be reached at 3.5 to 4 km depth (e.g. Friedleifsson and Elders, 2005).

Recent numerical simulations have demonstrated for the first time that the occurrence of exploitable supercritical reservoir is realistic under specific conditions (Scott et al., 2015). In particular, this study highlights the dominant role of the permeability and mechanical properties of rocks in the development of transient but large supercritical fluid volumes. In Iceland, the long term Iceland Deep Drilling Project (IDDP) proposes a direct approach for looking for these unconventional resources. A first well, IDDP-1, was drilled in 2009 in the Krafla area reaching a magma body at a depth of 2.1 km. Super-heated steam was extracted at a temperature near 450°C and the potential available power was estimated to 40-50 MW. More

recently, a second well, IDDP-2 drilled at the tip of the Reykjanes peninsula into the sheeted dike complex of the mid-ocean ridge, reached a depth of 4.6 km and a temperature of ~ 450°C (Friðleifsson et al., 2017).

Localization of potential sites for geothermal exploitation requires an accurate description of the reservoir based on combined geophysical and petrophysical investigations. In such extreme conditions, physical properties of fluid-saturated rocks are poorly constrained; identification of these reservoirs is often ambiguous and may lead to misinterpretation of geophysical signals as it was the case for IDDP-1 hole, where an unexpected magmatic intrusion was encountered.

Common geophysical methods used in geothermal exploration are based on electromagnetic investigations from shallow depths (Electrical Resistivity Tomography) to deeper parts using Transient Electromagnetic and Magnetotelluric methods. Indeed, electrical properties of rocks are dependent on fundamental parameters such as water presence, rock-type, temperature, pressure, porosity, pore connectivity and alteration mineralogy. Electrical soundings combined with borehole geophysics demonstrated that a classical geothermal reservoir displays a succession from top to bottom of a near-surface, poorly altered low conductive formation (< 0,01 $S.m^{-1}$) followed by a conductive body composed of altered rocks belonging to the smectite-zeolite facies (>0,1 $S.m^{-1}$), and finally followed by a low conductivity zone (<0,1 $S.m^{-1}$), corresponding to the highest degree of alteration (chlorite-epidote zone) and possibly leading to a decrease in fluid conductivity due to the presence of superheated steam (e.g. Arnason et al., 1987, Arnason, 2010, Gasperikova et al., 2015). This zone is classically the target production zone in Iceland, having temperatures between 250°C and 300°C. Investigations at higher pressures show an increase of conductivity with depth; in particular from 4 to 8-15 km where wide conductive bodies (>0,1 $S.m^{-1}$) have been identified beneath several geothermal areas in Iceland, such as Hengill geothermal area (e.g., Arnason et al., 2010) and Namafjall area (e.g. Karlsdottir et al., 2015). Because of high thermal gradients and active volcanic activity, these high conductivity zones can be attributed to either the presence of partial melting or to the presence of supercritical fluids (e.g. Jousset et al., 2011). On one hand, seismic investigations, especially beneath Hengill geothermal area, do not reveal any presence of velocity anomalies consistent with magma occurrence within these conductive body (Tryggvason et al., 2002, Jousset et al., 2011, Arnason et al., 2010), discarding the possibility of a molten rock body at depth. On the other hand, porosity and permeability are supposed to be relatively small at these depths, in particular in the vicinity of the brittle to ductile transition (>500-600°C) below which fluid presence and circulation is limited (Violay et al., 2012, Violay et al., 2015, Scott

et al., 2015). Up to now, no qualitative and quantitative data are available to describe the electrical signature of rocks under these extreme conditions where the presence supercritical fluids is suspected. Indeed, up to date laboratory investigations are limited to 200°C and show that electrical conductivity of these altered rocks is dominated by surface conductivity (i.e. alteration mineralogy) rather than by the electrolytic conduction. (Flovenz et al., 2005, Kristindottir et al., 2010, Levy et al., 2016).

In order to quantify the electrical signal of Icelandic crustal rocks at water supercritical conditions and to contribute to a better interpretation of the geophysical surveys, we present a series of electrical conductivity measurements performed on hydrothermally altered rocks, extracted from deep boreholes located in Reykjanes and Hengill geothermal areas. These rocks have been chosen due to their high temperature alteration (chlorite-epidote-amphibole zone) and their location close to IDDP targets. Our measurements were performed at a constant confining pressure of 130 MPa, at pore fluid pressures up to 30 MPa, and at temperatures up to 700°C. These conditions correspond to conditions that can be potentially found in supercritical reservoirs down to 4-5 km depth, such as the one recently drilled during IDDP-2 operations (e.g. Friðleifsson et al., 2017). In order to discriminate different conduction processes from each other, experiments were first performed under dry conditions to evaluate the intra-mineral contributions and then under pore-fluid saturated conditions with different fluid conductivities in order to identify the respective role of surface conduction and electrolytic conduction as a function of temperature.

2. Processes affecting electrical conduction at high temperature.

It is well established that the bulk electrical conductivity of rocks is the sum of the respective contributions of the electrolytes present in the porous media, of the rock/fluid interface known as surface conduction and of the intra-mineral conduction (Waxman and Smits, 1968), see Figure 1. Variation of rock conductivity may be described as follow, following the simplified Waxman and Smits (1968) relation generally valid for moderate to high fluid salinities and assuming that each conduction process operates in parallel:

$$\sigma_r(T,P) = \frac{\sigma_f(T,P)}{F(T,P)} + \sigma_s(T,P) + \sigma_{minerals}(T,P) \qquad \text{eq. (1)},$$

where at the rock scale, the successive terms are related to fluid, surface and intra- mineral conductions respectively are equal contributors. σ_r is the bulk electrical conductivity of the saturated rock, σ_f is the fluid

conductivity, F is the formation factor that describes the topology of the porous medium, σ_s is surface conductivity, and $\sigma_{minerals}$ represents intra-mineral conduction.

These parameters are all temperature and pressure dependent. These dependences are poorly constrained due the limited number of experimental electrical conductivity studies at high pressure and temperature conditions (Glover et al., 1992, Kummerow and Raab, 2015, Violay et al., 2012). This lack of data is partially due to the difficulty in pore pressure confinement while measuring electrical conductivity.

Pore fluid contribution

The electrolytic conductivity contribution is described by the first term $\frac{\boldsymbol{\sigma_f(T,P)}}{\boldsymbol{F(T,P)}}$ in equation (1) and depends on the fluid conductivity $\sigma_f(T,P)$ itself and on the formation factor $F(T,P)$ that represents the pore structure and connectivity. The dependence of pore fluid conductivity on salinity, pressure and temperature is well constrained up to 400 MPa and 600°C (e.g.; Quist and Marshall, 1968, Ucok et al., 1980, Kummerow and Raab, 2015), while there are recent studies that even go up to 4 GPa and 1400°C (Sinmyo and Keppler, 2017). In its liquid state, water conductivity increases almost linearly from 25 °C to 200°C. This is related to the rapid decrease of water viscosity, which results of an increase of ionic mobility. In this temperature range, temperature dependence of fluid conductivity (σ_F) is linear and can be written as:

$$\sigma_F(\mathrm{T}) = \sigma_F(T_0)\,(1 + \alpha_F(T - T_0)) \qquad \text{eq. (2).}$$

Revil et al., (1996) reported that the rate in which water conductivity ($\boldsymbol{\sigma}_F$) increases is nearly constant and independent of the fluid salinity, with α_F=0.023 K^{-1}. At temperature higher than 250°C, the rate of viscosity decrease is reduced and so is the change in ionic mobility. In addition, the decrease of isobaric density reduces the number of ions per unit volume and decreases the dielectric permittivity. These two processes dominate the viscosity effect. This decrease is more abrupt as fluid pressure decreases, leading to very low conductivity at pressures near supercritical point pressure (Sinmyo and Keppler, 2017, Quist et Marshall, 1968). On the opposite, as fluid pressure increases, electrical conductivity of NaCl-aqueous fluids become nearly constant with temperature at temperatures higher than 400°C and depends mostly on salinity, as reported by Quist and Marshall (1968) at 400 MPa, or in experiments on brine-bearing quartzite at 1 GPa and up to 800°C

by Shimojuku et al., 2012 and Shimojuku et al., 2014.

Surface conductivity

Surface conductivity is the result of electrochemical interactions between negatively charged mineral surfaces and ions present in saturating fluids. This mechanism acts within the so-called double layer formed by the surface charge layer (adsorbed ions) and the surface attracted ions layer (via Coulomb force). Its value (surface conductivity) depends on surface charge density, on the mineral surface area exposed to the fluid, on the cationic exchange capacity of the minerals and on the mobility of the surface ions. Alteration minerals such as smectite and zeolite, which display high exchange capacity, lead to a significant surface conductivity when present in rocks (e.g. Pezard, 1990). The transition from smectite to chlorite/epidote and actinolite alteration mineralogy leads to a drastic decrease in surface conduction, as these minerals have a much lower cationic exchange capacity than smectite (e.g. Flovenz et al., 2005, Kristindottir et al., 2010, Levy et al., 2016).

Temperature variation of the surface conductivity σ_S is considered to be linear up to 200°C, which can be expressed with the following equation:

$$\sigma_S(T) = \sigma_S(T_0).(1+\alpha_S(T-T_0)) \quad \text{eq. (3)},$$

Where α_S is generally higher than the temperature dependence of the pore fluid conductivity, making the surface contribution increasingly important at high temperature (Revil et al., 1998, Kristindottir et al., 2010). At higher temperatures, contribution of surface conduction has never been addressed. Glover and Vine (1994) compared the electrical behavior of saturated fresh granite (no alteration minerals) and amphibolite at temperatures up to 900°C. In granites, they found a decrease of the electrical conductivity above 350°C that has been attributed to a decrease of pore fluid conductivity at the liquid –supercritical transition, in agreement with pure electrolyte properties. On the opposite, in amphibolite the conductivity steadily increases with temperature. This has been tentatively explained by contribution of both intra-mineral and surface conductivity, which increase with temperature. But no quantification of the processes has been proposed yet.

Mineral conductivity

The intra-mineral contribution is represented by the third term in equation (1) namely $\sigma_{minerals}$ and is often regarded to play a minor role at low temperature conditions and in most of geothermal reservoirs (i.e.

temperature below 300°C). Indeed, dominant primary magmatic minerals present in magmatic rocks, such as olivine, pyroxenes and plagioclases, exhibit very low conductivities (< ~10^{-6} S/m) at temperatures lower than 400°C (e.g., Yang and MacCammon, 2012, Yang et al., 2012 for augite and plagioclase). However, the variation of electrical conductivity with temperature in the presence of high temperature alteration minerals, such as chlorites, epidotes and amphiboles that are encountered in hydrothermal systems, is poorly studied. Although these minerals exhibit low conductivities below 400-500°C (< ~10^{-4} S/m), they display a deep modification of their electrical behavior due to destabilization processes such as dehydration in undrained conditions. Strong effects have been evidenced in chlorite (Manthilake et al., 2016) and amphibole-bearing rocks (Fuji-ta et al., 2011, Wang et al., 2012), where the fluid released from dehydration reactions may act as a fluid conductor in the rocks, but also leads to oxidation reactions that modify the conductivity of iron-rich minerals. Such processes may enhance the electrical conductivity of bulk rocks at temperatures higher than 500°C by several orders of magnitude.

Finally, another possible effect related to electrical conduction in fluid-rock assembly concerns the fluid wetting properties, especially in a multiphase configuration. Some authors attempted to investigate the impact of the dihedral angle at the triple junction between grains boundaries and the fluids interface (e.g., Mibe et al., 1999 and Manthilake et al., 2015). They showed a net influence varying with temperature and pressure. In our present study, the experiments will be performed at fully saturated and monophasic conditions, where such effects will not be of concern.

3. Samples

Five samples from four boreholes of the active hydro-geothermal reservoirs located in Reykjanes (RN-17B, RN-19 and RN-30) and Nesjavellir (NJ-17) (Iceland) geothermal areas were investigated (Figure 2). They were classified as altered hyaloclastites (RN-17B, NJ-17B), dolerites (RN-19, RN-30) and basalts (NJ-17).

Sample paragenesis was determined by XRD analysis. Chemical composition of starting materials and post-experiments samples were determined by point analysis on thin-sections by Electron MicroProbe Analysis (EMPA) using a CAMECA SX100 microprobe. Cationic Exchange Capacity (C.E.C) was measured on powders using the Cobaltihexamine method at the *Laboratoire d'analyses des Sols* (Arras, France). Sample lithology and mineralogy are presented in Table 1.

Initial sample porosity and electrical properties were determined at room pressure and temperature conditions on cylindrical samples of 25.4mm in diameter and 20 to 40 mm in length. The porosity ϕ was measured by the triple weight method on dry, saturated, and immersed in water samples.

Where $\phi = (M_{sat}–M_{dry})/ (M_{sat}–M_{in})$, where M_{sat}, M_{dry} and M_{in}, correspond to the saturated, dry and immersed mass.

Formation factor *(F)* and surface conductivity *(Cs)* were determined by measuring the complex impedance of samples as a function of the conductivity of the pore saturating fluid. Fluid conductivity was changed by modifying the NaCl concentration (e.g. Pezard, 1990). Impedance was measured as a function of frequency using a two-pole configuration with a Solartron 1260 impedancemeter. For a given sample, petrophysical properties were determined on 5 to 8 cores and all samples were cored in the same direction. The relationship between the bulk rock conductivity and fluid conductivity was fitted with Waxman and Smits (1968) relation given by equation 1 in order to calculate the formation factor and the surface conductivity. The electrical tortuosity τ, corresponding to the product of the formation factor (F) and the porosity (ϕ), was also calculated. It relates to the geometrical complexity of the pore network followed by the electrical current into it.

Dolerite RN-19: RN-19 cores were taken from depths of 2238 – 2248m and at an *in-situ* temperature of 320°C (Fridleifsson et al., 2010). The selected sample originates from 2246.2 m depth. It is a fresh dolerite that is interpreted as a part of the sheeted dyke complex. The texture is coarse-grained with magmatic plagioclases and clinopyroxene phenocrysts (0.5 to 1 mm, Figure 3a). Plagioclase phenocrysts are zoned anorthites with An90 to An36 compositions, and clinopyroxenes are normally zoned augite to pigeonite in composition ($Wo_{40}En_{48}Fs_{11}$ to $Wo_{19}En_{28}Fs_{45}$ and mg# = 0.86 to 0.36 from core to rim, where mg#=Mg/Mg+Fe_{total}), see Table 1. Alteration is low with clinozoisite, actinolite, Fe-rich chlorite, talc, quartz and oxides (<10%). The initial porosity (given in Table 2) is distributed within inter- and intra-granular cracks that are thought to be mostly produced during drilling operation, i.e. cooling and decompression. This porous network leads to a relatively high electrical formation factor (see Table 2), which combined with a very low porosity indicates a relatively low tortuosity and good connection between pores. According to a low Cation Exchange Capacity (CEC), this rock displays a low surface conductivity at ambient conditions (0.4mS.m^{-1}).

Dolerite RN-30: RN-30 drill cores were taken at about of 2240 m of true vertical depth and at an in-

situ temperature of about 345°C (e.g. Fowler et al., 2016). The sample is classified as altered microdolerite with plagioclase and clinopyroxene microcrysts (Figure 3b). Plagioclase crystals are zoned from An81 to An76 and clinopyroxenes are augitic in composition ($Wo_{37}En_{49}Fs_{14}$ to $Wo_{39}En_{29}Fs_{32}$; mg#= 0.78-0.48). Secondary minerals are ferri-epidote, actinolite, quartz and oxides, while intensive chloritization is found in veins and cracks (Figure 3b). Electrical formation is high while porosity is slightly higher than the one observed in RN-19 (see Table 2). According to a low CEC, the surface conductivity is low.

Hyaloclastite RN-17B: This sample is a shallow marine volcanoclastic or hyaloclastic breccia drilled at a true vertical depth of about 2560 m and at an in-situ temperature of 345°C (Friedllifsson et al., 2010). It shows a high degree of alteration in epidote-amphibolite facies (Marks et al., 2011). It displays a fine-grained inhomogeneous texture containing a groundmass and vesicular blasts (Figure 3c). Plagioclase (An30- An6) and clinopyroxene occur as microlites in the groundmass alongside oxides and titanite. Amphiboles are magnesio-hornblende and are present by acicular needles, while ferri-epidote fills up pores and veins. Presence of amphibole reveals alteration temperatures higher than 400°C (Fowler et al., 2015), followed by a cooling episode revealed by epidote presence. Porosity is high and electrical formation is relatively low, while surface conductivity is low according to a low CEC (see Table 2).

Hyaloclastite NJ-17B: This altered hyaloclastite with high degree of chloritization was sampled at a depth of 1009 m (132 m below NJ-17). The groundmass contains fine-grained actinolite, chlorite, epidote, plagioclase (An66) and oxides. Large elongated pores are filled with chlorite, calcite and clinopyroxene ($Wo_{42}En_{43}Fs_{15}$ to $Wo_{43}En_{36}Fs_{21;}$ mg#=0.74-0.44) along the rims, and oxides and plagioclase in the pore centers. Irregular shaped oxide veins are present, extended by chlorite veins only. The presence of saponite has been determined by XRD analysis and is consistent with a significant CEC value of about 12 meq/100g, explaining the significant contribution of surface conduction, while electrical formation factor is relatively high (see Table 2 and Figure 3d).

Basalt NJ-17: This sample was cored at a depth of 877m in the Nesjavellir - Hengill geothermal field (132 m above NJ-17). It is an intensively altered basaltic lava with a porphyric texture of altered epidote and plagioclase (An30-An4) set in a fine-grained, not orientated dark brown groundmass, containing prismatic-needles of plagioclase and microcrysts of oxides and clinopyroxene ($Wo_{41}En_{45}Fs_{14}$ to $Wo_{30}En_{42}Fs_{28}$; mg#=0.77-0.61). XRD analyses indicate the presence of chlorite, quartz, calcite, and actinolite. Saponite, clay

from the smectite group, is also present, explaining the observed relatively high CEC, which reveals a complex alteration history from high temperature – actinolite zone to lower temperature alteration. Surface electrical conductivity is high, while formation factor is prominent, implying a relative high tortuosity given its high porosity (19%).

4. Methods: electrical conductivity at high temperature and pressure

Electrical conductivity measurements were conducted in the Paterson press at the Geosciences Laboratory of the University of Montpellier (France). This is an internally heated gas pressure vessel initially designed for high pressure (up to 500 MPa) and high temperature (up to 1300°C) deformation experiments. Electrical conductivity was measured under dry and saturated conditions, applying a 2-poles configuration on cylindrical samples and using a Solartron 1260 impedancemeter. In this configuration, the electrical conductivity is given as follows:

$$\sigma = \frac{R.L}{S} \qquad \text{eq. (4)},$$

where R is the measured resistance, S and L are the sample surface and length, respectively.

Under dry conditions, a simple setup based on the one described in Ferri et al. (2013; Figure 4a) was used. Electrical conductivity was measured in two parallel electrodes geometry mode (2-pole configuration) on cylindrical samples of 15 mm in diameter and 10-15 mm in length. Electrodes were made of nickel discs having a thickness and diameter of 0.2 mm and 15 mm, respectively. Ni electrodes have been chosen to buffer the oxygen fugacity close to the Ni-NiO buffer. Prior to the experiments, samples were cut and polished to obtain two parallel faces, and were dried at 70°C for at least 48 hours. Furthermore, the rock cylinders were surrounded by a porous alumina ring of 2.5 mm in thickness in order to insure an electrical isolation between the sample and the inox jacket that isolates the assembly from the confining medium. The confining pressure in the Paterson press was increased to 100 MPa and kept constant, while varying the temperature from room temperature up to 700°C. Different successive heating-cooling runs were performed with increasing maximum temperatures in order to investigate possible irreversible processes.

Under saturated conditions, the guard-ring method developed by Violay et al. (2012) was applied

(Figure 4b). This method allows the measuring of electrical conductivity of samples surrounded by a metallic jacket that separates the sample and the pore fluid from the confining pressure medium. Determination of the sample conductivity was performed similar to those under dry conditions. The cylindrical rock samples had a diameter of 22 mm and a length of 5 mm to 15 mm. They were sandwiched between 4 electrodes: two guard-rings and two nickel electrodes of 0.2 mm thickness supported by alumina and zirconia pistons. Grade-316 stainless steel tubes of 0.4 mm thickness were used as jacket material. The temperature was monitored by a sheeted K-type thermocouple, while the thermal gradient over the sample was small (<5°C over the sample length). The samples were vacuum-saturated with appropriate NaCl conductivities for at least one week prior to experiments in order to reach equilibrium. For each lithology, one sample was used per aqueous NaCl molality. The ambient electrolyte conductivities investigated were: very low conductivity [$\approx 10^{-3}$ S.m^{-1} to $1.5.10^{-2}$ S.m^{-1}], intermediate conductivity [0.12 S.m^{-1} to 0.13 S.m^{-1}] and near sea-water conductivity [3.36 to 7 S.m^{-1}]. Pore pressure was maintained at 25 MPa (at low salinity) or 30 MPa (at high salinity), confining pressure was kept constant at 100 MPa and temperature was varied from 25°C to 600°C.

The pore fluid system consisted of an automatic piston pump with 20cm^3 fluid capacity connected to the sample by high pressure pipes. The pore pressure was that of a closed-system, which did not allow any flow through the samples during measurements. Pore pressure was kept constant with an accuracy of 0.05 MPa, enabled by automatic displacement of the pore pressure pump piston. The absolute displacement of the piston depends on the cell temperature due to fluid dilatation, in particular at the transition from liquid to supercritical state, and was systematically measured during the conductivity measurements. Figure 5 shows (i) a calculation of the fluid expansion from equation of state for pure water taken from NIST database (Shen et al., 2006), an estimation of the pipe volume and temperature distribution within the cell from furnace calibrations while taking different samples porosities into account in respect to a 10 mm long sample, and (ii) measured fluid expansion as a function of temperature for different samples with variable porosities (for details see Fisher and Paterson, 1989). This Figure highlights a net increase of fluid volume into the cell along the phase transition range from liquid to supercritical state, and represents a good agreement between estimations and measurements on samples with different porosities. Low porosity samples RN-19 and RN-30 display limited expansion, which is consistent with calculations between 0 and 5%; whereas high porosity samples (NJ-17 and RN-17B) show higher expansions. This shows that the temperature and pore pressure

into the sample are well controlled, i.e. pore fluid into the sample is in equilibrium with the pipe and pump pressure (drained conditions).

Finally, in order to prevent time dependent effects (such as precipitations, salinity variation), each measurement step (steady-state conductivity versus temperature) was reached within 30 min on average. The equilibrium time was much larger for dry electrical measurements (1h on average).

Measurements and uncertainties

Uncertainties of electrical conductivity measurements derive from geometric factors and impedance measurements. Uncertainties in sample dimensions are relatively low and estimated to be less than 5%. Under saturated conditions, the sample length has an impact on the measured impedance due to electrical leakage at the sample borders in respect to the presence of the metallic jacket (accordingly to Violay et al., 2012). In particular, an overestimation of the conductivity results with increasing sample length. Based on calibration done on Fontainebleau Sandstone and by numerical simulations, this overestimation was quantified and a systematic correction was applied to the present measurements, depending on the samples length used.

Under dry conditions, impedance measurements as a function of frequency display a single impedance arc in the (Z', Z") plot and the sample resistance values are arbitrarily taken at the frequency with minimum quadrature component (Z") (example in Figure 6a for RN30). Under saturated conditions, a high frequency polarization impedance arc due to the Maxwell-Wagner effect is observed (e.g. Chelidze and Gueguen, 1999), while low frequency signals are affected by electrode polarization and other capacitive effects due to the metallic assembly used in this method (jacket and ends pistons), as shown in Figure 3b for RN17B. Resistance was systematically chosen at impedance measured at 1000 Hz, a domain were electrode polarization effects are estimated to be negligible. In order to quantify the uncertainty due to polarization effects, the impedance difference between 100 Hz and 10000 Hz was chosen as an absolute uncertainty. For all the measurements, this corresponds to about 5 to 30% of the measurement at 1000 Hz.

5. Results

Table 3 gives the experimentally determined parameters (C_w, E_a and α) for individual samples in respect to the run conditions (i.e. temperature, confining pressure, pore pressure and number of runs).

Dry conditions measurements

For all samples, a single impedance arc was observed in (Z', Z") plots, indicating a single conduction mechanism over the investigated frequency range (Figure 6a). The resulting conductivities are displayed in Figure 7. The measurements show a linear and reversible trend of the logarithm of rock conductivity as a function of T^{-1} up to 450-500°C for all samples. This overall behavior is consistent with an Arrhenius trend where one dominant conduction mechanism operates. The curves at low temperature (between 300°C and 500°C) in Figure 7 were fitted by the Arrhenius equation (equation 5).

$$\sigma(T) = A.e^{(-Ea/R.T)} \quad \text{eq. (5)},$$

where E_a is the activation energy and R the gas constant. The deduced apparent activation energies are given in Table 3. Except for the Hyaloclastite NJ17B with very low activation energy, all sample values are ~50±10 kJ.mol^{-1}. Above 500-600°C, an irreversible process increases the electrical conductivity with higher activation energies for samples RN17B and RN30 (see run3 for RN30 and RN17B in Figure 7). After reaching the maximum temperature, we performed new cooling-heating cycles, which display linear conductivity variation with temperature up to the maximum temperature. Conductivity values are systematically higher than the ones measured during the first heating run for these two samples. In contrary, samples NJ17, NJ17B and RN19 display a limited hysteresis.

Saturated condition measurements

Measured electrical conductivities of the five different samples as a function of temperature for different salinities are displayed in Figure 8. All curves can be described by a bell shape. This behavior mimics the water conductivity behavior with temperature (e.g. Quist and Marshall, 1968), where a maximum is observed in the interval 300-350°C under these pore fluid pressure conditions (25-30 MPa). Electrical conductivity increases systematically with initial fluid conductivity and salinity as expected. Measurements at high salinity in NJ17 and NJ17B, having very similar initial fluid conductivities, show similar values within the error bars, showing good reproducibility of the measurements.

The increase of rock conductivity with fluid conductivity is particularly significant in samples where initial surface conductivity was low, i.e. where electrolyte conduction is more dominant (RN19, RN30 and RN17B). In contrary, samples having a large initial surface conductivity show modest conductivity variations as a function of water salinity, especially for samples NJ-17 and NJ17B. In this case, the surface conductivity clearly dominates the overall rock conductivity.

In the temperature range of 25-150°C, and for all the samples, the increase in conductivity is nearly linear according to the fluid conductivity evolution with temperature (e.g. Quist and Marshall, 1968). Whereas between 200-350°C, the electrical conductivity is nearly constant, varying by about +/-0.2 log units. A decrease of conductivity is observed at temperatures above 350°C, leading to stabilizing conductivities reaching a minimum at about 500°C. This decrease is related to (i) a decrease of the water/charge carrier density where a large fluid expansion is shown in this temperature interval (Figure 5), and (ii) to a lowering of the dielectric constant of the fluid (e.g. Quist and Marshall, 1968). This decrease is about one order of magnitude for high initial water salinity. At temperatures higher than 500°C, a plateau or a slight increase in conductivity is generally observed where the conductivity of the saturated rock converges towards the conductivity of the dry rock (see samples NJ17, RN17B and RN30 in Figure 8).

Generally, dolerites (RN30 and RN19), having a low porosity, a large formation factor and low surface conductivity at ambient conditions, exhibit the lowest conductivity at high salinity, which is about one order of magnitude lower than for samples having a high-CEC (NJ17 and NJ17B) or a low formation factor (RN17B). At low salinity, these differences are becoming more important as surface conduction is much lower in dolerites than in hyaloclastites.

6. Discussion: electrical conductivity mechanisms.

Dry conditions: intra-mineral conduction.

The relatively low electrical conductivity values and low activation energies found in dry conditions measurements suggest electrical conduction via Fe^{2+}-Fe^{3+} electron transfers in ferrous minerals such as augite, amphibole and chlorite. Indeed, Manthilake et al. (2016) reported for chlorite bearing rocks activation energies of 27kJ.mol^{-1} up to 350°C and of 53 kJ.mol^{-1} from 350°C to 650°C. While Wang et al. (2012) and

Schmidbauer et al. (2000) have reported activation energy of about 65 kJ.mol^{-1} for amphibole-bearing rocks. Absolute conductivity values of the least altered sample RN19 is about one order of magnitude higher than for dry augite measured by Yang and MacCammon (2012), see comparison on Figure 7 - RN19 sample. Additionally, these values are at least one order of magnitude higher than for hydrated plagioclase measured by Yang et al. (2011), see Figure 7. This indicates that plagioclase contribution cannot explain the measured conductivity, while augite is probably the main contributor. Augites from RN19 are represented by $Fe_t/(Fe_t+Mg)$ ratios ranging from 0.2 to 0.6 (calculated from ferrosilite and enstatite contents in Table 1), which in average is higher than the value of 0.28 observed in the augite investigated by Yang and Mccammon (2012). In this mineral, where Fe^{2+}-Fe^{3+} charge transfers governs electrical conduction, a higher iron concentration may explain the higher electrical conductivity values observed in our measurements. In chlorite-rich samples, electrical conductivity is also higher by about one to two orders of magnitude than the ones reported by Manthilake et al. (2016). In this study, the investigated chlorite has a $Fe_t/(Fe_t+Mg)$ ratio of 0.246, while our altered rocks show a ratio of about 0.5 (Table 1), possibly explaining the observed discrepancies in absolute values. Finally, altered rocks of the amphibole-epidote facies (50% amphibole, 17% epidote; namely RN17B) are in a good agreement with our measurements of electrical conductivity and the hornblendite measured by Wang et al. (2012), see Figure 4. The average $Fe_t/(Fe_t+Mg)$) measured in their samples (0,48 to 0,51) is similar to the one found in RN17B (0.4-0.47) (Table 1). Regarding epidote, recent data have shown conductivities higher by 0.5 orders of magnitude for epidotes than for amphiboles measured up to 500°C (e.g., Wang et al., 2012, Hu et al., 2017).

The irreversible increase of conductivity observed above 500°C on RN17B and RN30 can be to the results of two distinct phenomena:

(1) ***Dehydration of water rich minerals and conduction of the released fluid***: powder XRD analyses and thin-section analyses of post-run samples have shown the destruction of chlorite structure. In low-permeability rocks, the resulting dehydrating fluids can be transiently stored in the pore space (grain boundaries, micro- cracks) through an interconnected network, leading to an increase of conductivity (e.g. Manthilake et al., 2016). However, given the relatively high permeability of these samples under the same P-T conditions (Nono et al., 2016); the fluid released from minerals is able to escape from the rock into the porous alumina surrounding the sample. For instance, sample RN17B, which clearly shows a strong

increase in conductivity, is highly permeable (1 milliDarcy) under the same conditions (Nono et al., 2016), where the released fluid could not be stored in the pore space even for very short durations.

Nevertheless, a small portion of the release fluids could have been retained or trapped in corners or crevices of the pore network between grain boundaries. Depending on the wetting properties of these fluids, i.e. their dihedral angles (Mibe et al., 1999, Manthilake et al., 2015), the interconnectivity between such fluids patches can result in an enhancement of the bulk rock electrical conductivity, and thus explained the observed hysteresis as the fluids remain connected at low temperatures. Note that measurements of the dihedral angles were not conducted in this study.

(2) ***Oxidation***: dehydrogenation at high temperatures leads to oxidation of iron-bearing minerals, following the reaction:

$Fe^{2+} + (OH)^{-} = Fe^{3+} + O^{2-} + 1/2\ H_2$

Where hydroxyl $(OH)^{-}$ is bound to Fe^{2+} in the stable structure. As mentioned by Schmidbauer et al. (2000) and Wang et al. (2012), oxidation between 500°C and 600°C leads to a conductivity increase as Fe^{3+}-Fe^{2+} charge transfer in hornblendes is increasing. Samples RN17B and RN30 contain significant proportions of amphibole (Table 1). While in RN17B, amphibole is so dominant (40 vol.%) that it forms a continuous matrix within the rock. Dehydrogenation and increase in Fe^{3+} content in amphiboles probably enhance the conductivity at temperatures higher than 500°C (Hui et al., 2017).

Regarding RN19, the very low content of alteration minerals explains the absence of irreversible change in conductivity. The matrix mineralogy of the two chlorite-rich samples NJ17 and NJ17B consists of less than 10% pyroxenes and amphiboles. The destabilization of chlorite can be observed from XRD patterns taken after experiments, but this has probably only a weak effect on the conductivity. Contrary to the study by Manthilake et al., (2016) where released fluids and magnetite formation increases the electrical conductivity, the released fluid has escaped from our samples and thus cannot contribute to conductivity.

Surface and electrolytic contributions under saturated conditions

The observed temperature and salinity dependences under saturated conditions suggest that even in samples where CEC and surface conductivity are low at room conditions the electrical conductivity is not solely

dependent on the electrolyte contribution (Figure 8). Along temperature range of 25-150°C, where the conductivity behaves linearly (Figure 8), the rate of conductivity increase (α) was calculated using equation (3) and is given in Table 3. This rate is systematically higher than the one expected for water only (i.e. 0.023 K^{-1} for the same temperature range). Similar rates were found in previous works for magmatic rocks (e.g. Flovenz et al., 1985, Kristindottir et al., 2010, Revil et al., 1996). These rates are explained by an increase in surface conduction due to an increase in ionic mobility in the electrical double layer of minerals surfaces. Thus, a clear dependence of surface processes on bulk rock conductivity is necessary to explain the conductivity evolution with respect to the temperature in saturated conditions. In the following, an estimation of the contribution of these processes to the conductivity is proposed by comparing bulk conductivity and electrolytic contributions. By subtracting intra-mineral and electrolyte conductivity to the measured conductivity, surface conductivity may be estimated (equation 1).

Intra-mineral contribution was evaluated from the electrical conductivity measured in dry conditions. Estimation of the electrolytic contribution is dependent on several assumptions and limitations. First, evaluation of electrolytic conductivity will depend on fluid chemistry and formation factor (equation 1). In saturated experiments, fluid conductivity may vary due to fluid-rock interactions (precipitation/dissolution processes). Under supercritical conditions, diffusion-controlled chemical reactions are particularly enhanced and favor mineral dissolution. On the other hand, the reduction of the dielectric constant of water leads to solid precipitation. These effects were clearly identified in long-term experiments (from days to weeks) on different Icelandic samples during flow-through experiments (e.g. Kummerow et al., 2016). While one week long experiments performed on basalts from Geitafell (Iceland) in sealed capsules at high temperature (>400°C) resulted in very modest fluid-rock alteration (Ruggieri et al., 2015). SEM images of our post-run samples do not show any visible mineralization within the pore space. EPMA data of mineral borders are not conclusive due to strong zonation found in the minerals of the initial rocks. The combination of short-term experiments (sample was kept only a few hours at high temperature), low fluid to rocks ratio, and sealed conditions greatly limit the fluid-rock interactions. In the following, this effect will be considered as negligible and fluid conductivity will be evaluated as a function of temperature by considering a constant concentration of charge carriers. The temperature dependence of fluid conductivity was extracted from Quist and Marshall measurements (1968) These measurements were found to be in good agreement with Sinmyo and Keppler (2017) formulations

The formation factor qualitative evolution during experiments can be indirectly estimated from permeability measurements on the same samples. Indeed, measurements of permeability on companion samples (Nono et

al., 2016) at high temperature and at similar effective pressures revealed that up to 250°C permeability decreases (slightly for RN-17B and more pronounced for NJ-17, NJ-17B, RN-19 and RN-30), which was also observed in the literature (e.g., Morrow et al., 1984, Zakir & Alan 2012). Above this temperature range, the permeability generally continues to decrease except for RN-19 for which an increase of more than two orders of magnitude is observed related to thermal cracking (Nono et al., 2016). For the others, as permeability decreases, formation factor increases. Over the whole range of temperature, if we calculate surface conductivity considering that formation factor is constant and equal to that at ambient temperature conditions (except for RN-19), we emphasize the fluid contribution (as F normally increases with temperature) and thus lower the surface conductivity values (see equation 1). We can then use this value of surface conductivity as a lower limit.

Permeability decreases much faster than formation factor increases (Kegang, 2012). Assuming a linear correlation between permeability and inverse of formation factor will lead to the prediction of an upper limit of surface conductivity as the formation factor values calculated will be above the true value and thus enhance surface conductivity.

In Figure 9, the evolution of surface conduction with temperature and with different ambient brine conductivities is shown for all samples, excepted for RN19 where large formation factor uncertainties were found due to high thermal cracking observed at high temperature (Nono et al. 2016). Surface conductivity has a similar behavior than water conductivity with temperature and increases with increasing ambient brine conductivity. Figure 9 shows that surface conductivity curves calculated from high initial salinity states samples lie above bulk saturated rock conductivity from low initial salinity state samples. It shows that surface conduction increases with salinity.

Surface conductivity almost increases linearly up to 250°C, reaching a plateau at 300°C and then decreases slowly. Between 100°C and 250°C, the slopes of the curves in Figure 9 are very similar for all samples. In addition, the bulk electrical and surface conductivity values of sample NJ17B are almost in the same range independently on salinity (Fig. 9d). Indeed, this sample presents the highest value of CEC and initial surface conductivity, while its electrolytic conduction is low.

Taking into account the contribution of mineral conductivity of dry experiments at high temperature (equation 1), the lower limit of surface conductivity contribution is calculated by assuming a constant formation factor. The results for high salinity measurements are plotted in Figure 10. Specific contributions of electrolyte, minerals and surface conduction are shown in Figure 10.

Figure 10 shows that electrolytic contribution drastically decreases above 350°C and becomes negligible at temperature higher than 400°C. On the other hand, surface conduction increases from room temperature to high temperature and becomes even dominant at temperature higher than 200-300°C, depending on the sample. At low temperature, the electrolyte conduction is dominant for rocks with low CEC (Fig. 8b and d, 10a and b) and low formation factor, e.g. RN17B. Even for rocks that have low CEC at ambient conditions, surface processes become efficient at high temperature. Although dominant, this contribution decreases with temperature from about 400°C to 600°C, where intra-mineral conduction starts to contribute significantly. However, given the phase diagram of the NaCl-water system defined by Driesner and Heinrich (2007), at a pressure of 300 bars, a temperature above 450°C and for high salinity experiments (seawater, 3%wt NaCl), the fluid is in a domain where vapor, liquid or halite in solid phase may coexist. In this domain, the pore fluid conductivity is more difficult to quantify and presence of halite precipitation may modify the electrical conductivity at temperature higher than 400°C. This possible effect is not enlightened in the present experiments. It could be addressed by varying pore pressure during experiments in order to explore different domains of the NaCl-water phase diagram. At temperature higher than 450°C, sample conductivity at high salinity may thus be dependent on possible modification of the fluid properties and not exclusively linked to surface processes. Regarding surface processes, they are the expression of an increase of local interactions and ionic exchanges between minerals surfaces and fluid. Figure 9 shows that these interactions are more pronounced with increasing fluid salinity, as surface conductivity strongly increases with salinity. Further investigations, in particular using flow-through experiments where fluid chemistry and fluid-rock interactions are more constrained compared to sealed experiments (e.g. Kummerow et al., 2016), would be necessary to accurately define the physical processes affecting the variation of electrical surface transport with temperature and salinity.

Conclusion: electrical conductivity of deep geothermal reservoirs.

Figure 11 summarizes the electrical behavior of different types of hydrothermally altered samples as a function of temperature. Up to 400°C-600°C, the electrical conduction is facilitated by the pore fluid through electrolytic and surface contribution. The transition temperature between the domains where fluid-assisted conduction (electrolytic and surface conduction) and intra-mineral conduction dominate strongly varies as a function of

lithology and fluid salinity. Rocks having a high formation factor, such as dolerites, display the lowest conductivity (curves d, e and h in Figure 11) and intra mineral conduction begins to contribute at about 400°C to 500°C, depending on the fluid salinity. Rocks with high surface contribution related to alteration minerals show a high electrical conductivity. This effect is enhanced by the fact that surface contribution increases with temperature. Maximum of conductivity is observed in the temperature range of 250°C-350°C, and a minimum is systematically observed at temperatures of 450°C-550°C. These temperatures are typical of those targeted by the IDDP project for exploration and exploitation of supercritical reservoirs. At higher temperatures, the conductivity increases because of intra-mineral conduction, which is mostly due to ferro-magnesian minerals such as chlorite, augite and amphibole (curves a, b and c in Figure 11). Destabilization of alteration minerals, in particular amphibole, leads to a non-linear and irreversible increase of conductivity (curve c in Figure 11). Alteration in the amphibole facies is the highest level of alteration found in Iceland, and the electrical behavior of this mineral may have an impact on the electrical signal at depth. Indeed, successive volcanic events in active rifts (e.g. Marks et al., 2011 for Reykjanes) constantly bury the rocks to greater depths and temperatures. The resulting destabilization of alteration minerals at temperatures higher than 500-600°C delivers one hypothesis for explaining an increase in conductivity below geothermal reservoirs and the formation of very large conductive bodies as observed by Arnason et al. (2010) at depths of 5- 9 km in the Hengill area or from 3-12 km in the Namafjall area (Karlsdottir et al. 2015), where typical conductivities are higher than 0.1 $S.m^{-1}$.

Comparison of experimental data to field observations may provide indications of fluid presence and nature at depth. The figure 11 reports three ranges of conductivity values provided by MT investigations: at a depth of about 3 to 4 km beneath the tip of the Reykjanes peninsula (blue area), beneath Hengill and Krafla geothermal areas at depth of about 1.5km, and at greater depth beneath Hengill and Namafjall geothermal areas.

Regarding Reykjanes area, at 3 to 4 km depth, formation temperatures are higher than 350°C (Friðleifsson et al., 2014). At these depths, the host rocks corresponds to a sheeted dyke complex composed of doleritic intrusions as observed in the IDDP-2 borehole down to 4.6 km depth (Friðleifsson et al., 2017). Analogs of these rocks are the doleritic samples RN-30 and RN-19. Comparison of conductivity values found from MT investigations at these depths (the blue area in figure 11, e.g. Friðleifsson et al., 2014) and laboratory experiments indicate that dry rocks can't explain the field observations (curve a, Figure 11). On the opposite, sea-water saturated doleritic rocks at temperature from 350 to 450°C provide very consistent electrical conductivities (curves h), indicating that presence of supercritical fluids may explain the field observations. This

consistency is in agreement with the presence of supercritical fluids at a minimum temperature of 425°C attested by the direct observations in the IDDP-2 borehole (Friðleifsson et al., 2017).

Beneath Hengill and Krafla areas, correlation between downhole temperatures and 3D magnetotelluric soundings indicate a wide body at temperatures between 250 and 350°C having conductivities ranging from 0,02 to 0,1 $S.m^{-1}$ (Gasperikova et al., 2015 – pink area on figure 11). This zone is situated at depths from 1 to 2 km and corresponds to the production zone. This range of conductivity is consistent with laboratory results with low salinity fluids (curve g in figure 11) i.e. fluids that are generally found in these geothermal areas where hydrothermal fluid is of meteoric origin (e.g; Kristindottir et al., 2010).

Finally, the wide conductive bodies found beneath the Hengill geothermal area at depths from 4 to 8 km (Arnason et al., 2010), and in Namafjall area at depth from 3 to 12 km (Karlsdottir et al. 2015) exhibit electrical conductivities higher than 0,1 $S.m^{-}1$. Seismic investigations beneath Hengill area have shown that these large bodies are not consistent with partially molten rocks (e.g. Tryggvason et al. 2002). Laboratory results indicate that fluid saturated rocks under supercritical conditions can explain such high conductivity values only, if low formation factor rocks (such as hyaloclastites) or if high salinity brines are considered (curve I, Figure 11). In addition, these conductivities intersect the dry conductivity curves at temperature higher than 800°C, indicating possible crystallized cooling intrusions that provide heat for the geothermal systems, as proposed by Arnason et al. (2010). Finally, destabilization of alteration minerals, such as chlorite or amphibole, which release conductive fluids at temperature higher than about 500°C-600°C, may also explain such high conductivities. Indeed, successive volcanic events in active rifts (e.g. Marks et al., 2011 for Reykjanes) constantly bury the rocks to deeper depth and temperatures. The resulting destabilization/dehydration of alteration minerals at high temperature delivers one hypothesis for explaining an increase in conductivity below these geothermal areas and the formation of very large conductive bodies. A similar hypothesis, based on laboratory measurements of electrical conductivity of hydrated phases, have been proposed to explain high electrical conductivity anomalies in the lower crust and subduction zone (e.g. Wang et al., 2012, Reynard et al, 2011, Manthilake et al., 2016 for amphibole, serpentine and chlorite dehydration, respectively) Further investigations, combining additional laboratory investigations and geophysical data are thus needed to discriminate such effects within the Icelandic mid crust.

Finally, Figure 11 displays the electrical conductivity of two types of magma of compositions that can be found in Icelandic context: a rhyolitic melt from Gaillard (2004), having a composition similar to the one found in Krafla area (e.g. Tuffen et Castro, 2009) or the one from by IDDP1 hole at 2.1 km depth (Zierenberg et al., 2013), and a basalt-olivine aggregate with different melt fractions from Laumonier et al. (2017). This figure shows that a pure basaltic melt at 1200°C has a conductivity value of about 0.5 $S.m^{-1}$, which is one order of magnitude higher than the maximum conductivity found in the present study, i.e. for high CEC rock samples saturated by a high salinity fluid at 250°C-350°C, see sample (i) in Figure 11. In addition, a partially molten peridotite containing 10% and 4% of basaltic melt has a much lower conductivity at 1200°C than a pure basaltic melt, having values similar to fluid-saturated rocks at 250-350°C. This similarity is also found when one compares the conductivity of a rhyolitic melt and fluid-saturated rocks. At lowest salinity, our samples have conductivities one to two orders of magnitude lower than magma conductivity, depending on rock type. The conductivity at 300°C for rocks altered within the chlorite facies, which contain small amount of smectite (e.g., NJ17 or NJ17B), may be similar to the one of cooling rhyolitic magmatic intrusions. Hence, it is difficult to image very recent magmatic intrusions within geothermal reservoirs at shallow depth, as it was the case in 2009 when a rhyolitic intrusion was drilled into at 2.1 km depth during the IDDP1 operation.

Acknowledgements

The research leading to these results has received funding from the European Community's Seventh Framework Program (FP7) under grant agreement no. 608553 (FP7 Project IMAGE). We are grateful to HS Orka power company for making IDDP core samples from the Reykjanes geothermal system available for scientific studies, and to the International Continental Scientific Drilling Program (ICDP) and the American National Science Foundation (NSF; grant no. 05076725) for their financial support in drilling cores at Reykjanes. Christophe Nevado and Doriane Delmas are thanked for thin-sections preparation, Pierre Azais and Nicolas Marino for their precious contributions at the High-Pressure Laboratory, Bernard Fraisse and Fabrice Barou for their assistance in XRD measurements and SEM observations, respectively, and Léa Lévy for XRD Rietveld refinements.

References

Árnason K., Flóvenz Ó., Georgsson L., and Hersir G.P., 1987: Resistivity structure of high temperature geothermal systems in Iceland. International Union of Geodesy and Geophysics (IUGG) XIX General Assembly, Vancouver, Canada, August, abstract V, 477.

Árnason K., Eysteinsson H., and Hersir G. P., 2010: Joint 1D inversion of TEM and MT data and 3D inversion of MT data in the Hengill area, SW Iceland, Geothermics, 39, 13-34.

Driesner, T. and Heinrich, C.A., 2007: The system H2O-NaCl. Part 1: Correlation formulae for phase relations in temperature-pressure-composition space from 0 to 1000° C, 0 to 5000 bar and 0 to 1 XNaCl, Geochimica et Cosmochimica Acta 71, 4880-4901, 2007.

Elders W.A., Friðleifsson G.O., and Albertsson A., 2014: Drilling into magma and the implications of the Iceland Deep Drilling Project (IDDP) for high-temperature geothermal systems worldwide, Geothermics, 49.

Ferri F., Gibert B., Violay M., Schilling F R., Cesare B., 2013: Electrical conductivity in a partially molten lower crust from measurements on xenoliths, Tectonophysics, doi.org/10.1016/j.tecto.2012.11.003.

Flóvenz Ó.G., Georgsson L.S., and Árnason K., 1985: Resistivity structure of the upper crust in Iceland, J.Geophys. Res., 90-B12, 10, 136-10,150.

Flóvenz Ó.G., Spangenberg E., Kulenkampff J., Árnason K., Karlsdóttir R. and Huenges E., 2005: The role of electrical conduction in geothermal exploration, Proceedings World Geothermal Congress 2005, Antalya, Turkey, CD, 9 pp.

Fournier R.O., 1999: Hydrothermal processes related to movement of fluid from plastic into brittle rock in the magmatic-epithermal environment, Economic Geology, 94, 1193-1211.

Fowler A.P.G., Zierenberg R.A., Schiffmann P., Marks N. and Friedlifsson G.O., 2015: Evolution of fluid–rock interaction in the Reykjanes geothermal system, Iceland: Evidence from Iceland Deep Drilling Project core RN-17B, Journal of Volcanology and Geothermal Research, 302, 47-63.

Fowler A.P.G., and Zierenberg R.A., 2016a: Elemental changes and alteration recorded by basaltic drill core samples recovered from in-situ temperature up to 345°C in the active, seawater-recharged Reykjanes Geothermal System, Iceland, G3, DOI 10.1002/2016GC006595.

Fowler, A.P.G. and Zierenberg, R.A., 2016b, Geochemical bias in drill cutting samples versus drill core samples returned from the Reykjanes Geothermal System, Iceland: Geothermics, 62, p. 48-60.

Friðleifsson G.Ó.,and Elders W.A., 2005: The Iceland Deep Drilling Project: a search for deep unconventional geothermal resources, Geothermics, 34, 269-285.

Friðleifsson G.Ó. and Richter B., 2010: The geological significance of two IDDP-ICDP spot cores from the Reykjanes geothermal field, Iceland. In: Proceedings of the World Geothermal Congress, Bali, Indonesia.

Friðleifsson, G. Ó., Sigurdsson, Ó., Þorbjörnsson, D., Karlsdóttir,R., Gíslason, Þ., Albertsson, A., and Elders, W. A.: Preparation for drilling well IDDP-2 at Reykjanes, Geothermics, 49, 119–126, 2014b.

Friðleifsson, G.Ó., Elders, W.A., Zierenberg, R.A., Stefánsson, A., Fowler, A.P.G., Weisenberger, T.B., Harðarson, B.S., Mesfin K.G., 2017. The Iceland Deep Drilling Project 4.5 km 1118 deep well, IDDP-2, in the sea-water recharged Reykjanes geothermal field in SW Iceland 1119 has successful reached its supercritical target. Scientific Drilling (in press)

Fuji-ta K., Katsura T., Ichiki M., Matsuzaki T., Kobayashi T., 2011: Variations in electrical conductivity of rocks above metamorphic conditions, Tectonophysics. 504 (1-4): 116-121.

Gaillard F., 2004: Laboratory measurements of electrical conductivity of hydrous and dry silicic melts under pressure, Earth and Planetary Science Letters, 218 (1-2), 215-228.

Gasperikova E., Rosenkjaer G., Arnason K., Newman G. and Lindsey N., 2015: Resistivity characterization of the Krafla and Hengill geothermal fields through 3D MT inverse modeling, Geothermics, 57, 246–257.Glover P.W.J., and Vine F.J., 1994: Electrical conductivity of the continental crust, Geophys. Res. Lett., 21, 2357-2360.

Hu H., Dai L., Li H., Hui K., and Sun W., 2017: Influence of dehydration on the electrical conductivity of epidote and implications for high-conductivity anomalies in subduction zones, J. Geophys. Res. Solid Earth, 122, 2751–2762, *doi:*10.1002/2016JB013767.

Hui K., Dai L., Li H., Hu H., Jiang J., Sun W., and Zhang H. 2017: Experimental Study on the Electrical Conductivity of Pyroxene Andesite at High Temperature and High Pressure. *Pure and Applied Geophysics*, *174*(3), 1033-1041.

Jousset P., Haberland C., Bauer K., and Arnàson, K., 2009: Detailed structure of the Hengill geothermal volcanic complex, Iceland, inferred from 3D tomography of high-dynamic broadband seismological data. Geothermics IGET, Special Issue.

Karlsdóttir R., Vilhjálmsson A. M. and Teklesenbet A., 2015. Námafjall High Temperature Field in N Iceland. A 3D Resistivity Model Derived from MT Data. Proceedings of the World Geothermal Congress, Melbourne, Australia.

Kegang L., 2012: Correlation between Rock Permeability and Formation Resistivity Factor-A Rigorous and Theoretical Derivation., SPE Middle East Unconventional Gas Conference and Exhibition, 23-25 January 2012, Abu Dhabi, UAE 2012.

Kristinsdóttir L. H., Flóvenz O. G, Árnason K., Bruhn D., Milsch H., Spangenberg E., and Kulenkampff J., 2010: Electrical conductivity and P-wave velocity in rock samples from high-temperature Icelandic geothermal fields,Geothermics, 39(1), 94 –105.

Kummerow J., Raab S., 2015: Temperature dependence of electrical resistivity – Part I: Experimental investigations of hydrothermal fluids. Energy Procedia 2015; 76: 240-246.

Kummerow, J., Raab, S., 2016: Physical properties of rocks and aqueous fluids at conditions simulating near- and supercritical reservoirs, EGU, Vienna.

Laumonier, M., Farla, R., Frost, D.J., Katsura, T., Marquardt, K., Bouvier, A-S., Baumgartner, L.P. ,2017. Experimental detemerination of melt interconnectivity and conductivity in the upper mantle, Earth Planet. Scl. Lett., 121 (1).

Lévy L., Flóvenz Ó. G., and Hersir G. P., 2016: IMAGE Task 3.3 - Physical Properties of Rock at Reservoir Conditions - Quantitative Impact of Hydrothermal Alteration on Electrical Resistivity, based on cores from Krafla, Iceland GeoSurvey, ÍSOR-2016/043.

Manthilake, G., Mookherjee, M., Bolfan-Casanova, N., and Andrault, D. 2015: “Electrical Conductivity of Lawsonite and Dehydrating Fluids at High Pressures and Temperatures.” Geophysical Research Letters 42: 7398-405.

Manthilake G., Bolfan-Casanova, N., Novella, D., Mookherjee, M., Andrault, D., 2016: Dehydration of chlorite explains anomalously high electrical conductivity in the mantle wedges, Sci. Adv. 2016; 2: e1501631.

Marks N., Schiffman P. and Zierenberg R.A., 2011: High-grade contact metamorphism in the Reykjanes geothermal system: Implications for fluid-rock interactions at mid-oceanic ridge spreading centers. Geochemistry, Geophysics, Geosystems, vol. 12, 25 pp.

Mibe K, Fujii T, Yasuda A .1999) Control of the location of the volcanic front in island arcs by aqueous fluid connectivity in the mantle wedge. Nature 401:259-262

Morrow C.A., Moore D.E., and Byerlee J.D., 1984: permeability changes in crystalline rocks due to temperature: effect of mineral assemblage, Mater. Res. Soc. Symp. Proc., 26, 883-890.

Nono F., Gibert B., Parat F., Loggia D, Azais, P., Cichy, S.B., 2016: Permeability of Icelandic deep geothermal reservoirs: insight from HT-HP experiments, EGU 2016, Vienna.

Pezard P.A., 1990: Electrical properties of mid-ocean ridge basalt and implications for the structure of the upper oceanic crust in Hole 504B.J. Geophys. Res., 95:9237-9264.

Revil A., Darot M., Pezard P. A., and Becker K., 1996: Electrical conduction in oceanic dikes, hole 504B, in Alt J. C., Kinoshita H., Stokking L. B., and Michael P. J., eds., Proceedings of the Ocean Drilling Program, scientific results: vol. 148, Ocean Drilling Program, 297–305.

Revil A., Cathles III L. M., Losh S., Nunn J. A., 1998: Electrical conductivity in shaly sands with geophysical applications, J. Geophys. Res., 103, 23.

Reynard, B., K. Mibe, and B. van de Moortele, 2011. Electrical conductivity of the serpentinized mantle and fluid flow in subduction zones, Earth and Planetary Sciences Letters, 307, 387-394.

Ruggieri G., Orlando A., Chiarantini L., Montegrossi G., Rimondi V., Borrini D. and Weisenberger T. B., 2015: Fluid-rock interaction experiments to investigate super-hot geothermal reservoirs, Mid-Term-Conference, Integrated Methods for Advanced Geothermal Exploration Pisa 12-13/10/2015.

Schmidbauer E., Kunzmann T., Fehr T., Hochleitner R., 2000: Electrical resistivity and 57Fe Mössbauer spectra of Fe-bearing calcic amphiboles. Phys Chem Miner 27:347–356.

Scott S., Driesner T., and Weis P., 2015: Geological controls on supercritical resources above magmatic intrusions, Nature, DOI: 10.1038/ncomms8837.

Shen, V.K., Siderius, D.W., Krekelberg, W.P., and Hatch, H.W., Eds., NIST Standard Reference Simulation Website, NIST Standard Reference Database Number 173, National Institute of Standards and Technology, Gaithersburg MD, 20899, http://doi.org/10.18434/T4M88Q

Shimojuku, A., Yoshino, T., Yamazaki, D. and Okudaira T., 2012. Electrical conductivity of fluid-bearing quartzite under lower crustal conditions, Physics of the Earth and Planetary Interiors, 198-199: 1-8.

Shimojuku, A., Yoshino, T. and Yamazaki, D., 2014. Electrical conductivity of brine-bearing quartzite at 1GPa: implications for fluid content and salinity in the crust, Earth, Planets and Space, 66:2.

Sinmyo R and H Keppler, Electrical conductivity of NaCl-bearing aqueous fluids to 600C and 1 GPa, Contrib. Mineral Petrol, 172(4), 2017

Taut R., Kleenerg R., Bergmann J., 1998: The new Seifert Rietveld program BGMN and its application to quantitative phase analysis Materials Science, **5**, pp. 55–64.

Tryggvason, A., Rögnvaldsson, S.T., Flovenz, O.G., 2002. Three-dimensional imaging of the P and S-wave velocity structure and earthquake locations beneath Southwest Iceland. Geophysical Journal International 151, 848–866.

Ucok H., Ershaghi I., and Olhoeft G., (1980). Electrical resistivity of geothermal brines. Journal of Petroleum Technology, 34, 04.

Violay M., Gibert B., Azais P., Lods G., Pezard P.A.., 2012: A new cell for electrical conductivity measurement on saturated samples at upper crust conditions, Transp Porous Media doi 10.1007/s11242-011-9846.

Violay M., Gibert B., Mainprice D. and Burg J.-P., 2015: Brittle versus ductile deformation as the main control of the deep fluid circulation in oceanic crust. Geophys. Res. Lett. 42, 2767–2773.

Wang D., Guo Y., Yu Y. and Karato S., 2012: Electrical conductivity of amphibole bearing rocks: Influence of dehydration, Contributions to Mineralogy and Petrology, in press.

Waxman M.H., and Smits L.J.M., 1968: Electrical Conductivity in Oil Bearing Shaly Sands, Society of Petroleum Engineers Journal, June, p.107-122.

Yang X., McCammon C., 2012: Fe3+-rich augite and high electrical conductivity in the deep lithosphere. Geology 40:131–134.

Yang X., Keppler H., McCammon C., Ni H., 2012: Electrical conductivity of orthopyroxene and plagioclase in the lower crust. Contrib Mineral Petrol 163:33–48.

Zakir H., Alan J. C., 2012: Relationship among porosity, permeability, electrical and elastic properties, SEG Las Vegas.

Zierenberg R.A., Schiffman P., Barfod G.H., Lesher C.E., Marks N.E., Lowenstern J.B., Mortensen A.K., Pope E.C., Fridleifsson G.Ó., Elders W.A., 2013: Composition and origin of rhyolite melt intersected by drilling in the Krafla geothermal field, Iceland. Contributions to Mineralogy and Petrology 165, 327–347.

Tables:

Table 1: Starting material, sample provenance, lithology, mineralogy (from XRD Rietveld analysis) and chemical analysis (EPMA) of dominant minerals. An# represent anorthite content in plagioclase, augite compositions are defined in the wollastonite (Wo)-enstatite (En)-ferrosilite (Fs) space. Fe number, defined as the ratio $Fe_t/(Fe_t+Mg)$, where Fe_t is the total iron content (by weight), is calculated for amphibole and chlorite.

	RN-19	**RN-30**	**RN-17B**	**NJ-17**	**NJ-17B**
Area	Reykjanes	Reykjanes	Reykjanes	Nesjavellir	Nesjavellir
True vertical depth	2246.2m	2240m	2560m	877m	1009m
In-situ T(°C)	320	345	345	230	230
Lithology	Dolerite	Dolerite	Hyaloclastite	Basalt	Hyaloclastite
Mineral content (% volume)					
Quartz	-	3.9	-	9	0.3
plagioclase	61.5	37.8	26.2	31.6	33.8
Augite	27.2	31.6	3.0	11.5	10
Saponite	-	-	-	9	12.1
Chlorite	5.7	11.7	-	31.1	22.8
Epidote	-	-	17.6	-	
Actinolite	3.7	9.1	-	1.8	6
amphibole	-	-	53.2	-	-
Titanite	-	<1	-	8.6	8.8
Calcite	-	-	-	-	2.5
grossular	-	-	-	-	1.8
Zeolite	1.5	-	-	-	1.1
Prehnite	-	3.6	-	-	-
Mineral chemistry of dominant minerals (% weight)					
Plagioclase	An90-An36	An81-An76	An30-An6	An60-An4	An66
Augite	$Wo_{40}En_{48}Fs_{11}$ to $Wo_{19}En_{28}Fs_{45}$	$Wo_{37}En_{49}Fs_{14}$ to $Wo_{39}En_{29}Fs_{32}$		$Wo_{41}En_{45}Fs_{14}$ to $Wo_{30}En_{42}Fs_{28}$	$Wo_{42}En_{43}Fs_{15}$ to $Wo_{43}En_{36}Fs_{21}$
Chlorite Fet/(Fet+Mg)	0.47	0.63-0.56		0.55-0.43	0.51-0.43
Epidote	clinozoisite	Ferri-epidote	Ferri-epidote		Ferri-epidote
Amphibole Fet/(Fet+Mg)	Actinolite 0.45	Actinolite 0.63	Hornblende 0.40-0.47		

Table 2: Petrophysical properties of starting materials at room conditions (standard deviation in bracket)

	RN-30	**RN-17B**	**NJ-17**	**NJ-17B**
Porosity Φ (%) and standard deviation	3.3 (+/-0.4)	13.4 (+/-2.8)	19.4 (+/-1.4)	12.3 (+/-1.8)
Formation Factor F and standard	559(+/-80)	64(+/-12)	102 (+/-18)	138(+/-30)
*Tortuosity (=F*Φ)*	18.4	8.3	19.8	17.0
Surface conductivity ($S.m^{-1}$) C_S and standard deviation	6.10^{-4}(+/-2)	$5.4.10^{-4}$ (+/-2)	$3.5.10^{-3}$ (+/-0.9)	$9.5.10^{-3}$ (+/-2)
CEC (meq/100g)	2.37	<1	11.9	10.7

Table 3: Description of experiments and experimentally determined temperature-dependent parameters: P_C is the confining pressure. P_F is the pore fluid pressure. $C_{W.0}$ is the conductivity of saturating fluid at ambient condition. E_a is the activation energy calculated for dry experiments (equation 4). and α is the rate of rock conductivity increase in the temperature range 25-200°C for saturated experiments (equation 3) – see text for details.

	P_C (MPa)	P_F (MPa)	T range (°C)	$C_{W.0}$ ($S.m^{-1}$)	E_a ($KJ.mol^{-1}$)	α (25-150°C) (K^{-1})
RN19-1	100	-	300-650	-	59.2	
RN30-1	100	-	200-700	-	42.7	
RN17B-1	100	-	200-700	-	63.6	
NJ17-1	100	-	200-700	-	51.5	
NJ17B-1	100	-	200-700		21.8	
RN19-2	100	25	25-450	$0.55.10^{-3}$		0.0566
RN19-3	100	30	25-600	7.04		0.0228
RN30-2	100	25		$1.2.10^{-3}$		0.0448
RN30-3	100	30	25-600	3.56		0.0495
RN17B-2	100	25	25-450	$0.92.10^{-3}$		0.0392
RN17B-3	100	25	25-450	$2.3.10^{-3}$		0.0245
RN17B-4	100	25	25-600	$14.8.10^{-3}$		0.0236
RN17B-5	100	30	25-600	0.130		0.021
RN17B-6	100	30	25-600	6.46		0.0257
RN17B-7	100	30	25-600	3.23		0.0502
NJ17-2	100	25	25-450	$1.04.10^{-3}$		0.0925
NJ17-3	100	25	25-600	$14.2.10^{-3}$		0.0657
NJ17-4	100	30	25-600	0.126		0.0777
NJ17-5	100	30	25-600	4.3		0.0243
NJ17-6	100	30	25-600	3.6		0.0407
NJ17B-2	100	30	25-600	0.101		0.0335
NJ17B-3	100	30	25-600	3.36		0.0471
NJ17B-4	100	30	25-600	3.92		0.0621

Figures

Figure 1: Different conduction mechanisms in a fully saturated rock.

Figure 2: Borehole locations and simplified stratigraphy of the four boreholes from Friedlifsson et al., 2014 and Fowler and Zierenberg, 2016b. Dotted lines on Icelandic map delineate volcanic systems (Reykjanes and Hengill).

Figure 3: Microstructures and mineralogy of starting materials: microphotographs from Scanning Electron Microscope.

Figure 4: Sketch of the devices used for measuring electrical conductivity under dry (a) and saturated (b) conditions (from Ferri et al., 2013 and Violay et al., 2012).

Figure 5: Effect of temperature on fluid expansion in the conductivity cell showing the transition from liquid to supercritical conditions. Dotted lines represent calculations of fluid expansion based on fluid volume exposed to high temperature in the cell (including pores in the samples and pipes) and on the temperature distribution. Different sample porosities (in %) have been tested. Continuous lines show results of direct measurements of fluid volume variation in the cell for different experiments (see text for details).

Figure 6: Impedance arcs at different temperatures under dry and saturated conditions for samples RN30 and RN17B.

Figure 7: Electrical conductivity under dry conditions for the five samples and comparison with electrical conductivity obtained in rocks or synthetic aggregates (plagioclase from Yang et al., 2011; augite from Yang and McCammon. 2012; hornblende from Wang et al., 2012).

Figure 8: Electrical conductivity measurements under saturated conditions as a function of fluid salinity. For comparison measurements under dry conditions are systematically given.

Figure 9: Lower and upper limits of the surface conductivity estimated by considering constant formation factor and linear relationship with inverse of permeability respectively.

Figure 10: On the right. separate contributions of the electrolyte surface and intra-mineral conductivities to the bulk rock conductivity and on the left, contribution in % of minerals (dry conductivity) and surface conductivity to the bulk conductivity that considers pore fluid conductivity, surface conductivity and mineral conductivity. Contributions are calculated assuming constant formation factor with temperature.

Figure 11: Electrical conductivity of Icelandic crustal rocks at high temperature: (a) relatively fresh dolerite sample RN19. (b) amphibole-bearing sample RN17B and (c) chlorite-bearing sample NJ17. Dotted line displays electrical conductivity under saturated conditions at low salinity for doleritic samples (e) RN19 and (d) RN30, for (f) hyaloclastite RN17B and (g) hyaloclastite NJ17. Large dotted line includes in light grey (h) measurements at near sea-water salinity on high formation factor samples (dolerites) and in black (i) on samples having a high surface conductivity and/or a low formation factor (hyaloclastites). Conductivity of relevant melt composition is also given: (j) a dry olivine-MORB mixture at 1.5 GPa from Laumonier et al., (2017) with different melt contents (100%. 10% and 4% from top to bottom). and (k) a dry rhyolitic melt at 50 MPa from Gaillard et al. (2004). The blue and pink areas delineate conductivity values reported from MT investigations beneath the tip of the Reykjanes peninsula (IDDP-2 location) and in the production zone of the Hengill and Krafla geothermal areas (temperature of 250-350°C) respectively (Gasperikova et al., 2015 and Friðleifsson et al., 2014). The red area corresponds to deep seated conductive bodies found in Hengill and Namafjall geothermal area (Karlsdottir et al. 2015. Arnason et al, 2010).

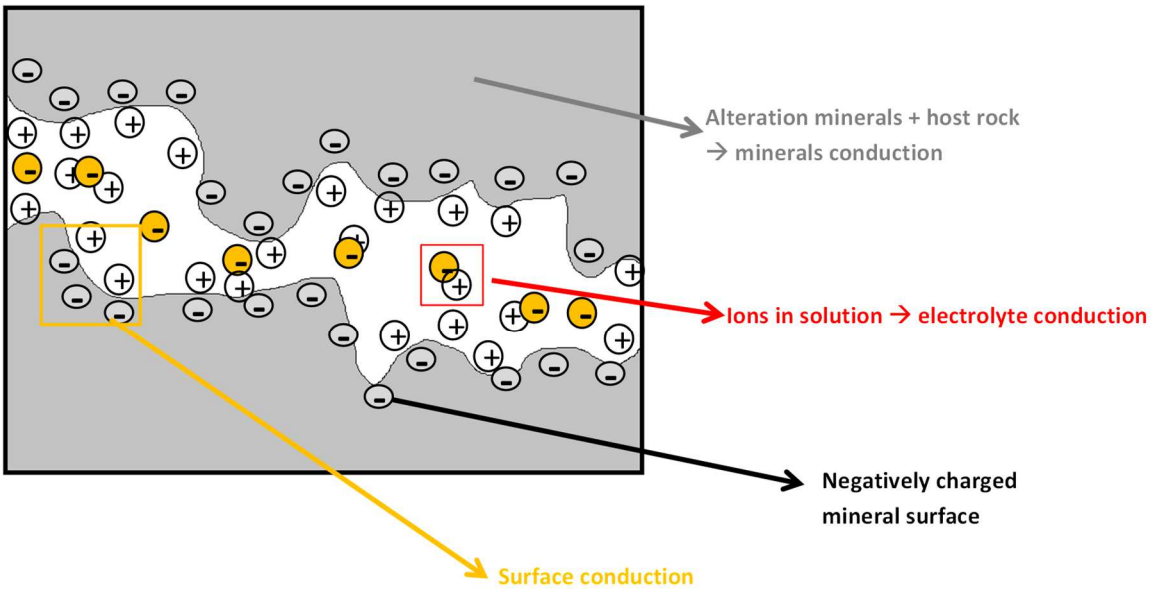

Figure 1: Different conduction mechanisms in a fully saturated rock

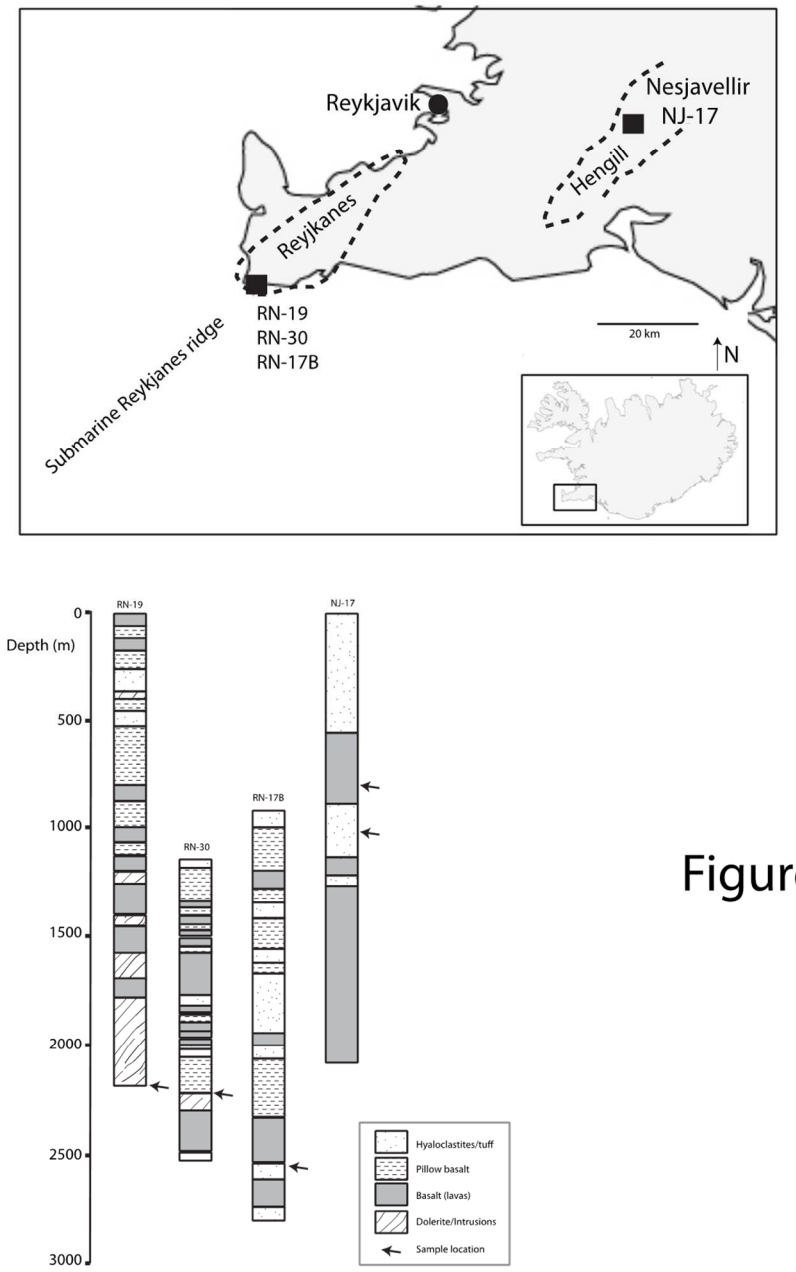

Figure 2

Figure 2: Borehole location and simplified stratigraphy of the four boreholes from Friedlifsson et al., [2014] and Fowler and Zierenberg [2016b]. Dotted lines on Iceland map delineate volcanic systems (Reykjanes and Hengill).

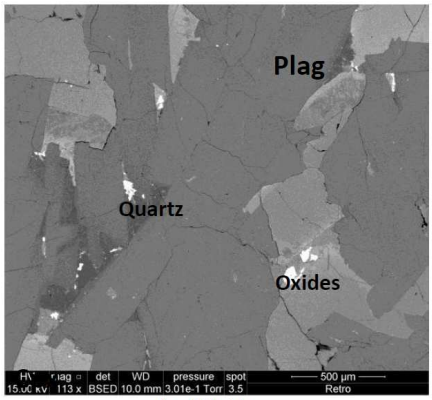

a) RN-19

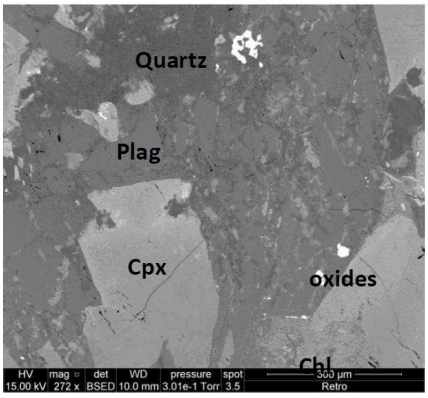

b) RN-30

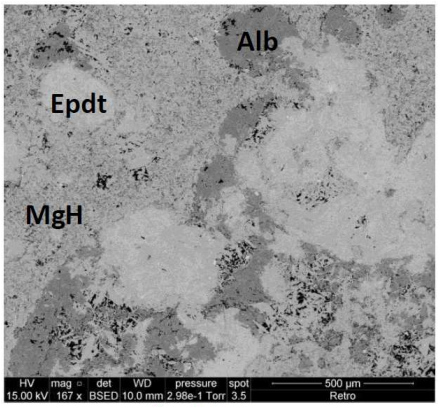

c) RN-17B

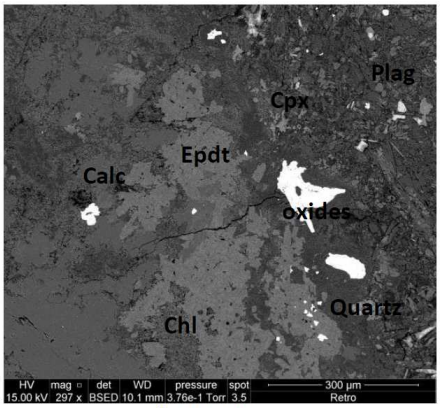

d) NJ-17B

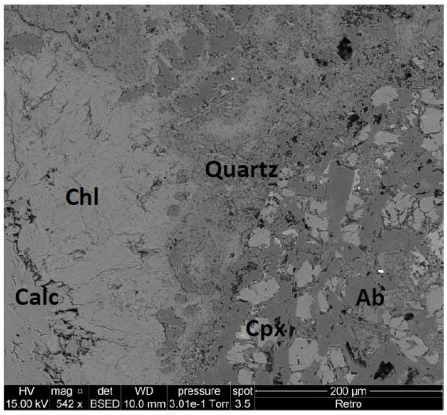

e) NJ-17

Ab = Albite

Calc = Calcite

Chl = Chlorite

Cpx = Pyroxene

Epdt = Epidote

MgH = Magnesiohornblende

Plag = Plagioclases

Figure 3: Microstructures and mineralogy of starting materials: microphotographs from Scanning Electron Microscope.

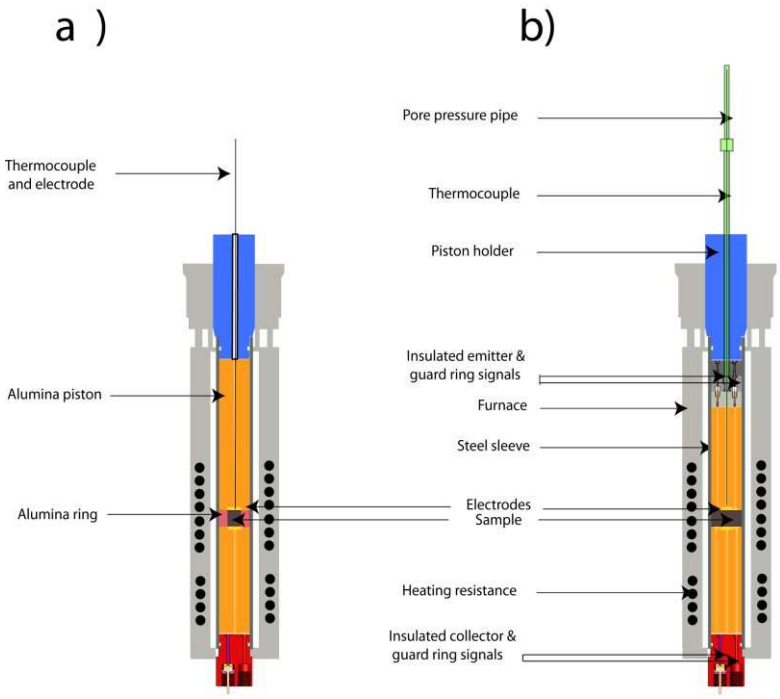

Figure 4: Sketch of the devices used for measuring electrical conductivity under dry (a) and saturated (b) conditions (from Ferri et al., 2013 and Violay et al., 2012).

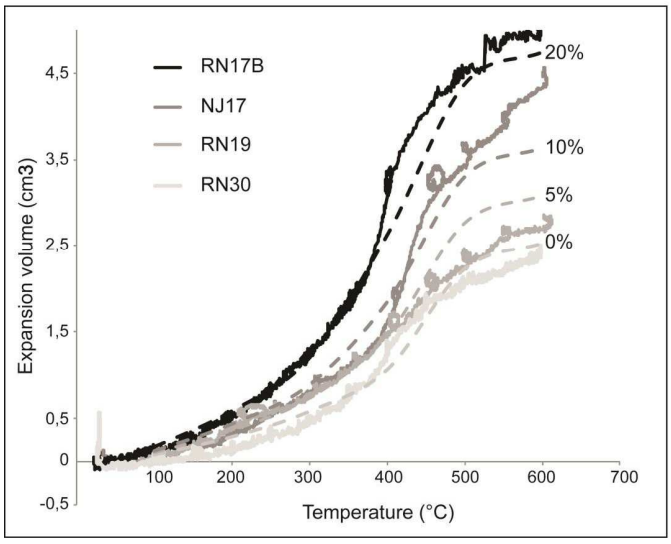

Figure 5: Effect of temperature on fluid expansion in the conductivity cell showing the transition from liquid to supercritical conditions. Dotted lines are calculations of fluid expansion based on fluid volume exposed to high temperature in the cell (including pores in the samples and pipes) and on the temperature distribution. Different sample porosities (in %) have been tested. Continuous lines are from direct measurements of fluid volume variation in the cell for different experiments (see text for details).

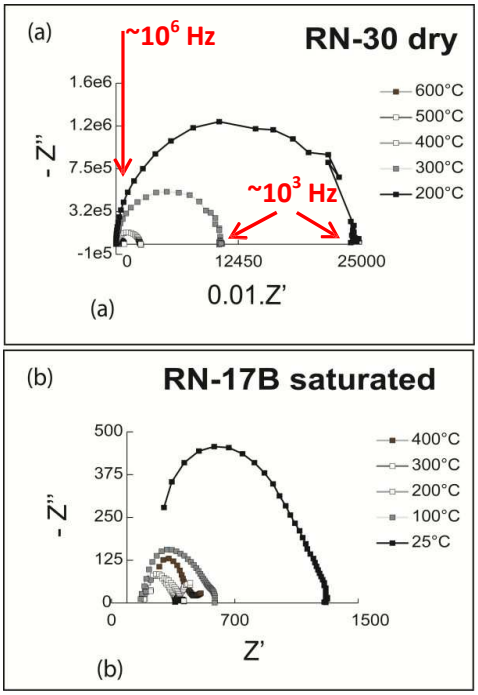

Figure 6: Impedance arcs at different temperatures under dry and saturated conditions for samples RN30 and RN17B.

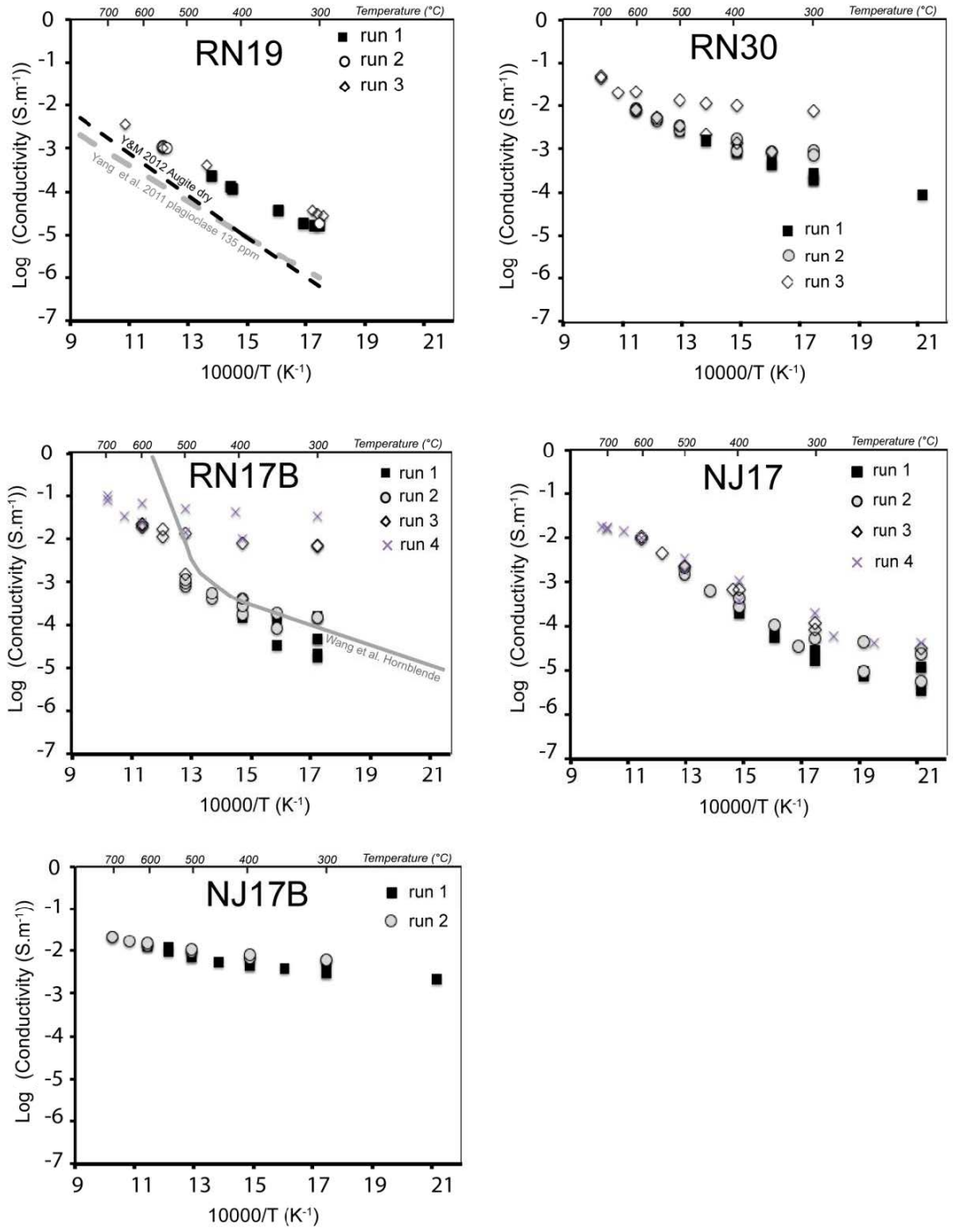

Figure 7: Electrical conductivity under dry conditions for the five samples and comparison with electrical conductivity obtained in rocks or synthetic aggregates (plagioclase from Yang et al., 2011; augite from Yang and McCammon, 2012, hornblende from Wang et al., 2012).

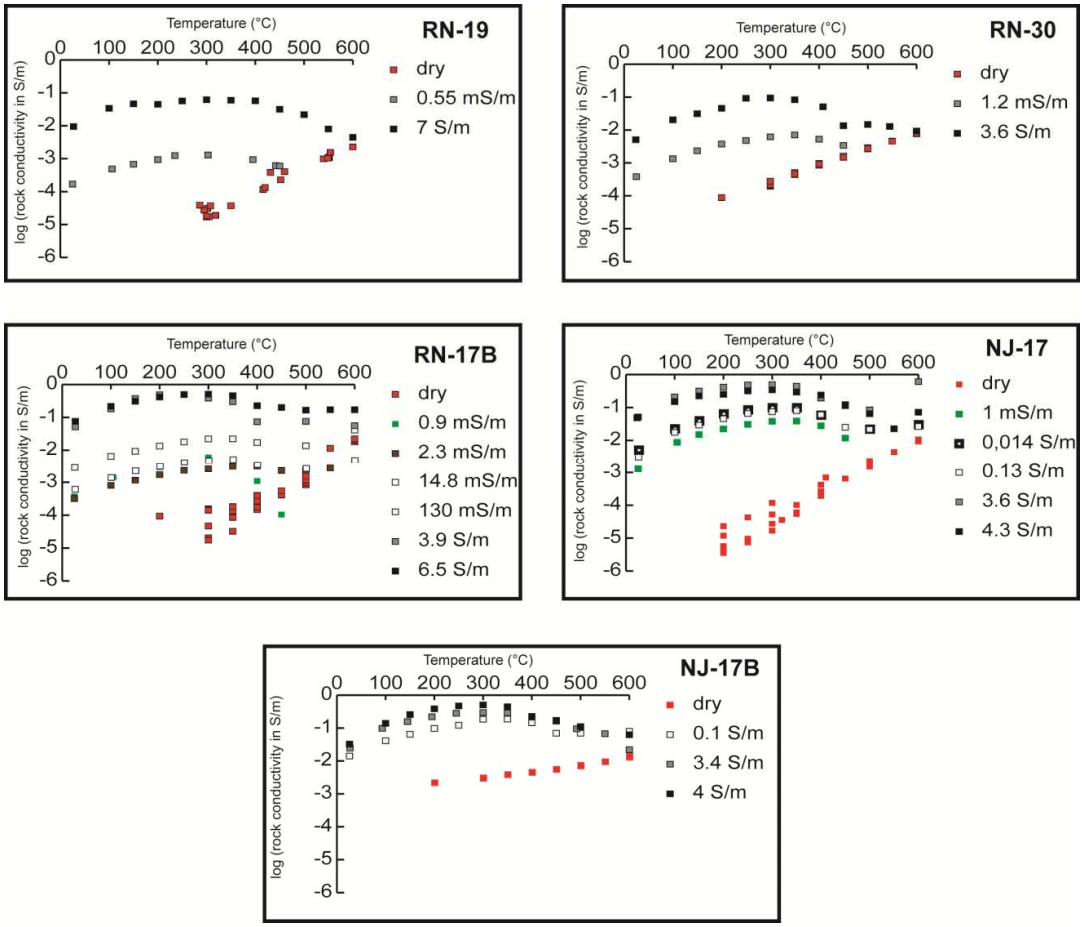

Figure 8: Electrical conductivity measurements under saturated conditions as a function of fluid salinity. For comparison, measurements under dry conditions are systematically given.

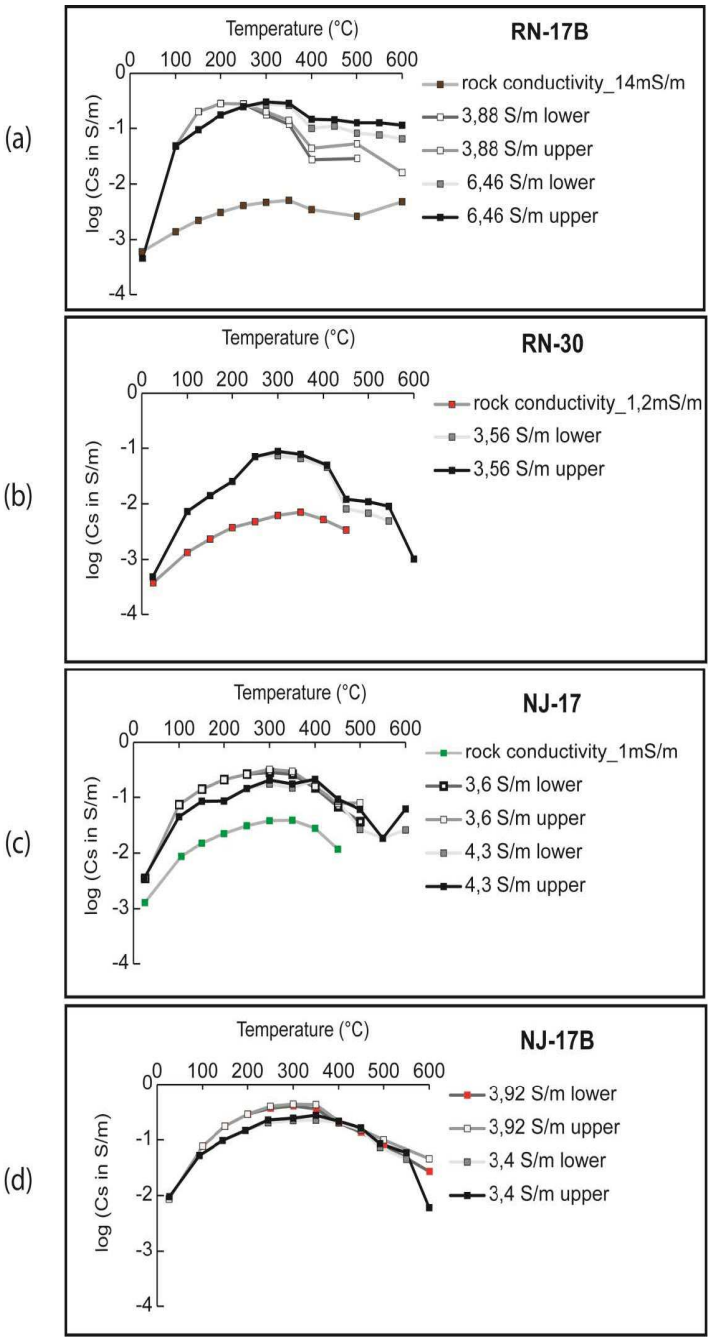

Figure 9: Lower and upper limits of the surface conductivity estimated by considering constant formation factor and linear relationship with inverse of permeability respectively.

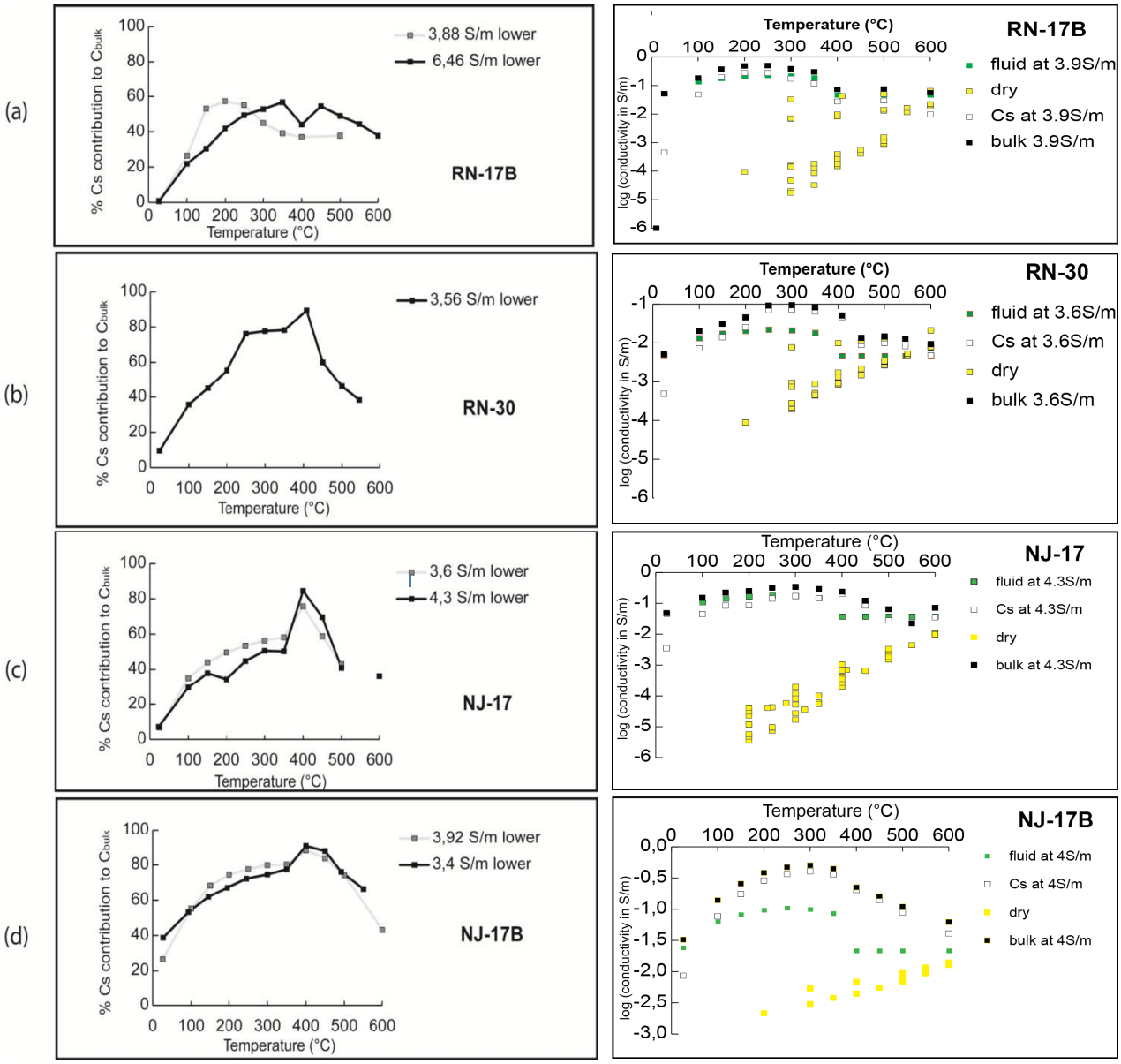

Figure 10: On the right, separate contributions of the electrolyte, surface and intra-mineral conductivities to the bulk rock conductivity and on the left, contribution in % of surface conductivity to the bulk conductivity that considers pore fluid conductivity. surface conductivity and mineral conductivity. Contributions are calculated assuming constant formation factor with temperature.

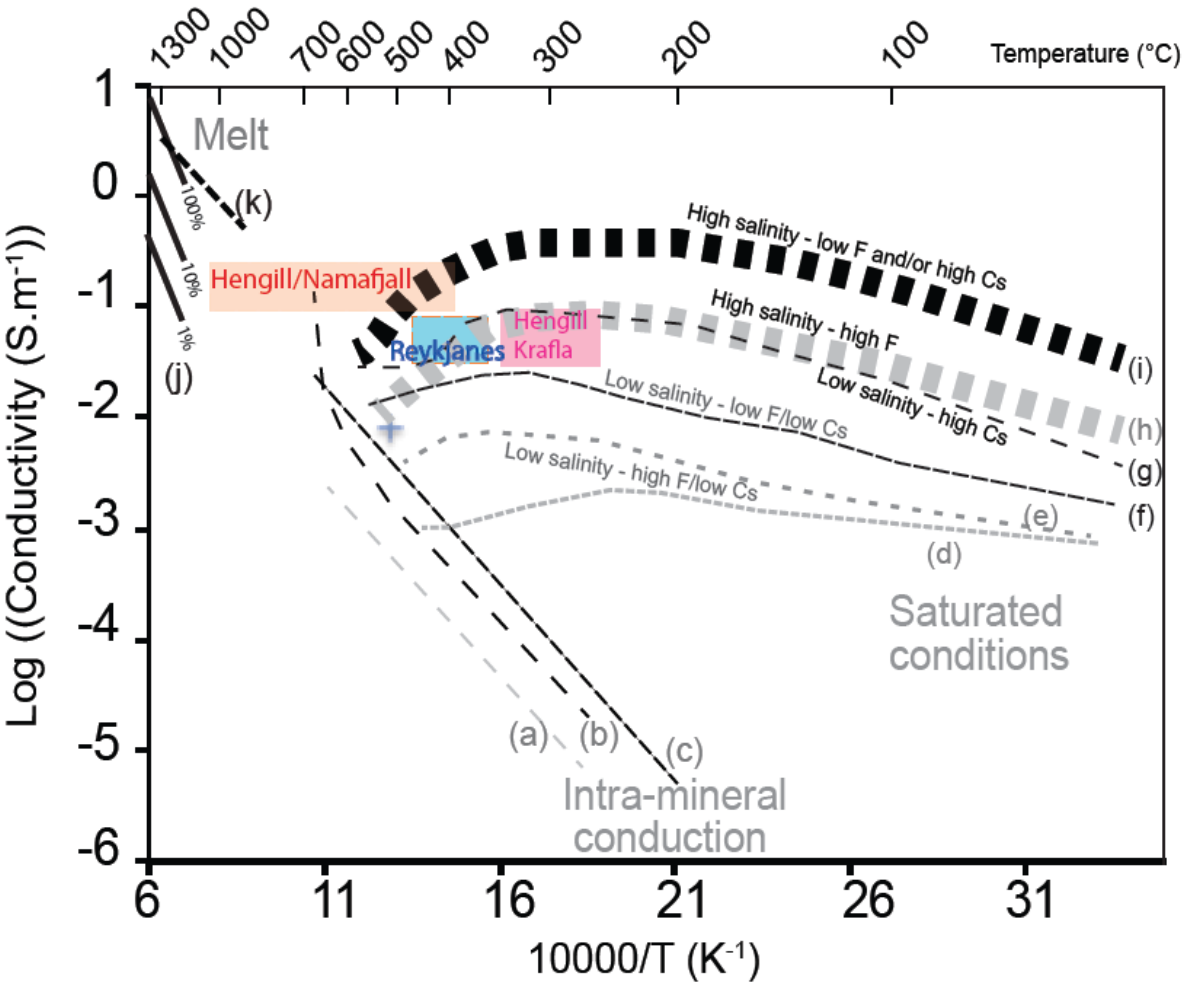

Figure 11: Electrical conductivity of Icelandic crustal rocks at high temperature. (a) Relatively fresh dolerite sample RN19. (b) amphibole-bearing sample RN17B. and (c) chlorite-bearing sample NJ17. Dotted line displays electrical conductivity under saturated conditions at low salinity for doleritic samples (e) RN19 and (d) RN30. for (f) hyaloclastite RN17B and (g) hyaloclastite NJ17. Large dotted line includes. in light grey (h) measurements at near sea-water salinity on high formation factor samples (dolerites) and in black (i) on samples having a high surface conductivity and/or a low formation factor (hyaloclastites). Conductivity of relevant melt composition is also given. (j) a dry olivine-MORB mixture at 1.5 GPa from Laumonier et al.. 2017 with different melt contents (100%. 10% and 4% from top to bottom) and (k) a dry rhyolitic melt at 50 MPa from Gaillard et al., 2004. The blue and red areas correspond to conductivity values reported from MT investigations beneath the tip of the Reykjanes peninsula (IDDP-2 location) and beneath the Hengill volcano respectively (Arnason et al., 2010 and Friðleifsson et al., 2014)